Research Square

Preprints are preliminary reports that have not undergone peer review.
They should not be considered conclusive, used to inform clinical practice,
or referenced by the media as validated information.

Electronic force fields and their associated local charge densities in small molecules featuring conventional covalent and charge-shift bonds and in contact ion pairs

Sergey V. Kartashov

Arbuzov Institute of Organic and Physical Chemistry, FRC Kazan Scientific Center, Russian Academy of Sciences

Robert R. Fayzullin

robert.fayzullin@gmail.com

Arbuzov Institute of Organic and Physical Chemistry, FRC Kazan Scientific Center, Russian Academy of Sciences

---

Research Article

Keywords: Atomic Slater force, Charge-shift bonding, Electronic force fields, Electron-pair-deficient covalent bonds, Exchange–correlation charge density, Interatomic charge transfer, Interatomic interactions, Pseudoatoms in molecules, Quantum chemical response, Source function of the static potential, Total atomic charge, Total static potential

Posted Date: November 27th, 2026

DOI: https://doi.org/10.21203/rs.3.rs-11873460/v1

License: This work is licensed under a Creative Commons Attribution 4.0 International License.
Read Full License

Additional Declarations: Competing interest reported. Sergey V. Kartashov declares no competing interests. Robert R. Fayzullin declares that he is a member of the Editorial Board of Structural Chemistry.

Electronic force fields and their associated local charge densities in small molecules featuring conventional covalent and charge-shift bonds and in contact ion pairs

Sergey V. Kartashov [1] and Robert R. Fayzullin [1] *

[1] Arbuzov Institute of Organic and Physical Chemistry, FRC Kazan Scientific Center, Russian Academy of Sciences, 8 Arbuzov Street, Kazan 420088, Russian Federation

* Email: robert.fayzullin@gmail.com

Abstract

This article first reviews the theoretical formalism based on electronic force fields and their associated local charge densities and identifies promising directions for further research. Within this framework, the Slater total static potential $\varphi_{\mathrm{em}}(\mathbf{r})$ acting on an electron in an N-electron chemical system is formally defined here by averaging the Coulomb interaction energy operator for electron i, $\hat{V}_i$, over the conditional probability distribution of the remaining $N-1$ electrons, given that electron i is at $\mathbf{r}$. This definition provides a rigorous basis for deriving chemically significant physical quantities. The article then presents quantum-chemical calculations at a correlated level of theory for LiF, LiH, HF, BN, CO, NO, N_2, N_2H_4, N_2O_4, H_2O_2, and F_2. Particular attention is given to the phenomena of interatomic electron transfer and consequent quantum chemical response, as revealed by the superposition of the electron density gradient field $\nabla\rho(\mathbf{r})$, the per-electron electrostatic force field $\mathbf{F}_{\mathrm{es}}(\mathbf{r})$, and the Slater total static force field $\mathcal{F}(\mathbf{r}) = -\nabla\varphi_{\mathrm{em}}(\mathbf{r})$. The analysis further addresses electron-pair density condensation and decondensation in the many-electron cloud, which are represented by regions where the Slater exchange–correlation charge density $q_{xc}(\mathbf{r}) = \nabla\cdot[\mathcal{F}(\mathbf{r}) - \mathbf{F}_{\mathrm{es}}(\mathbf{r})]/(4\pi)$ takes negative and positive values, respectively. Importantly, charge-shift bonding is shown to manifest itself in real space as electron-pair density decondensation within

internuclear binding regions, with this decondensation apparently driven by Coulomb correlation. On this basis, covalent bonds whose internuclear binding regions exhibit such decondensation, as indicated by positive values of $q_{xc}(\mathbf{r})$, are proposed to constitute a distinct class, here termed electron-pair-deficient covalent bonds. Finally, theoretical analysis of $\mathcal{F}(\mathbf{r})$ allows tensile and compressive principal modes of the local linear variation of the scalar Cartesian components of this force field to be distinguished along their respective principal directions. These modes are characterized by the eigenvalues of the Hessian of $\varphi_{\mathrm{em}}(\mathbf{r})$ at the corresponding saddle-type Lagrange point of $\mathcal{F}(\mathbf{r})$. In this context, the tensile principal mode is more pronounced relative to the compressive principal modes in charge-shift bonds than in conventional homoatomic covalent bonds, with the former representing attraction of the electron cloud toward the nuclei and the latter representing attraction of the electron cloud toward the bond axis. Thus, the force-field and charge-density perspective on chemical structure yields robust orbital-free descriptors of interatomic interactions, thereby enabling the charge-shift character of electron-pair-deficient covalent bonds to be captured and quantified outside the framework of valence bond theory.

Keywords

Atomic Slater force · Charge-shift bonding · Electronic force fields · Electron-pair-deficient covalent bonds · Exchange–correlation charge density · Interatomic charge transfer · Interatomic interactions · Pseudoatoms in molecules · Quantum chemical response · Source function of the static potential · Total atomic charge · Total static potential

Introduction

The present article continues and extends our previous investigations, which sought to understand chemical structure and interatomic interactions—a central problem in quantum chemistry—from a force-field and charge-density perspective [1–28]. It first reviews the relevant theoretical formalism and identifies promising directions for further research in the “Theoretical background” and “Theoretical framework” sections before turning to the investigation itself. Specifically, the analysis

focuses on a set of electrically neutral many-electron multinuclear systems examined *in vacuo* comprises lithium fluoride (LiF), lithium hydride (LiH), hydrogen fluoride (HF), boron nitride (BN), carbon monoxide (CO), nitric oxide (NO), dinitrogen (N_2), hydrazine (N_2H_4), dinitrogen tetroxide (N_2O_4), hydrogen peroxide (H_2O_2), and difluorine (F_2). Herein, the many-electron wave functions are calculated at a correlated level of theory. The first two species listed are tight ion pairs, each held together by a strong ionic bond with pronounced coordinative character. The next five are small diatomic molecules with varying degrees of ionic character in their covalent bonds. The final four species in the sequence are distinguished by increased electron deficiency within their central axial bonds. Such electron-deficient covalent bonds are now often discussed in terms of charge-shift bonding, in which Lewis-pair fluctuation within the internuclear region is proposed to play a decisive role in the underlying chemical-bonding mechanism, a role reflected in the dominant covalent–ionic resonance-energy contribution [29–33].[1] In the context of contemporary valence bond theory, the notion of charge-shift bonding has emerged as an extension of Lewis's paradigm of electron-pair bonds. This development calls for a more comprehensive investigation of the underlying phenomenon, particularly within an orbital-free conceptual framework [16]. It is worth noting that, within quantum crystallography [28], electron-deficient covalent bonds have also been studied on the basis of intracrystalline electron-density distributions reconstructed from X-ray diffraction data [34–37].

Theoretical background

A successful attempt to preserve the concept of the atom as a constituent of a Coulombic electron–nuclear system (*e.g.*, a molecule or a crystal) within a rigorous quantum-mechanical description was made by Bader and coworkers [38–43]. Their quantum theory of atoms in molecules is based on the

[1] Lewis-pair fluctuation is mentioned here solely to describe the interpretation advanced in the charge-shift bonding literature; the present authors do not regard such fluctuation (or charge shifting in this sense) as a physical phenomenon.

idea that the flux of the electron density gradient field $\nabla\rho(\mathbf{r})$ through certain boundaries that delimit chemically bonded atoms within the system is zero:

$$\nabla\rho(\mathbf{r}) \cdot \mathbf{n}(\mathbf{r}) = 0, \qquad \forall \mathbf{r} \in S(\Omega_S), \tag{1}$$

where $\mathbf{n}(\mathbf{r})$ is the unit normal vector to the corresponding zero-flux surface at each point $\mathbf{r}$. These boundaries, denoted S, enclose the atomic basins Ω_S. The condition expressed in Eq. (1), together with the resulting constraint given in Eq. (2), guarantees that the two integral representations of the kinetic energy of an atomic subsystem yield the same value [41, 43], as is the case for the system as a whole, despite the difference between the corresponding local Schrödinger and Lagrangian (gradient) kinetic energy densities. Atoms defined in this way are open quantum-mechanical subsystems to which Schwinger's principle of stationary action applies [41, 43–46]. In an equilibrium nuclear configuration, each atom identified with a basin Ω_S satisfies the usual integral form of the virial theorem because the corresponding nuclear virial term vanishes, thereby allowing the total energy of the system to be decomposed additively into atomic contributions [38, 41, 43, 47]. These fundamental properties are largely ensured by the atoms-in-molecules requirement, which serves as a constraint on the partitioning of electronic charge concentration [38]:

$$\iiint_{\Omega_S} \nabla^2\rho(\mathbf{r})\mathrm{d}\Omega_S = 0. \tag{2}$$

Here, $\nabla^2\rho(\mathbf{r})$ is the Laplacian of the electron density. Taken together, these features provide a physical basis for the chemically important concept of atomic charge defined in terms of the electron population of an Ω_S basin; this population corresponds to the expectation value of the number operator [48, 49]:

$$Q_{\nabla\rho} = \iiint_{\Omega_S} q_{\mathrm{es}}(\mathbf{r})\mathrm{d}\Omega_S = Z - \iiint_{\Omega_S} \rho(\mathbf{r})\mathrm{d}\Omega_S, \tag{3}$$

where $q_{\mathrm{es}}(\mathbf{r}) = \sum_n Z_n\delta(\mathbf{r} - \mathbf{R}_n) - \rho(\mathbf{r})$ is the electrostatic charge density, Z denotes the charge number of the nucleus enclosed within the basin under consideration, and $\rho(\mathbf{r})$ is the electron density.

Within this theory, a bond path—a pair of trajectory lines in the vector field $\nabla\rho(\mathbf{r})$, both originating at the same saddle-type equilibrium point and each terminating at a corresponding attractor, typically located at an atomic nucleus—is justifiably used as an indicator of chemical

bonding[2] between atoms in electron–nuclear systems at equilibrium [50–52]. As a quantitative measure of the interaction between any pair of atoms in the system, irrespective of whether they are in contact, the electron delocalization index $\delta\left(\Omega_S^{\mathrm{A}}, \Omega_S^{\mathrm{B}}\right)$ is often used. This index counts the number of electrons shared by the atomic basins Ω_S^{A} and Ω_S^{B} and can be expressed in terms of the exchange–correlation two-electron density $\Gamma_{xc}(\mathbf{r}, \mathbf{r}')$ [53–55]:

$$\delta\left(\Omega_S^{\mathrm{A}}, \Omega_S^{\mathrm{B}}\right) = -2 \int_{\Omega_S^{\mathrm{A}}} \int_{\Omega_S^{\mathrm{B}}} \Gamma_{xc}(\mathbf{r}, \mathbf{r}') \mathrm{d}\mathbf{r}' \mathrm{d}\mathbf{r}. \quad (4)$$

Note that $\Gamma_{xc}(\mathbf{r}, \mathbf{r}') = \Gamma_{xc}^{\uparrow,\mathrm{total}}(\mathbf{r}, \mathbf{r}') + \Gamma_{xc}^{\downarrow,\mathrm{total}}(\mathbf{r}, \mathbf{r}')$ is the Fermi–Coulomb contribution to the spin-summed two-electron pair density $\pi(\mathbf{r}, \mathbf{r}') = \rho(\mathbf{r})\rho(\mathbf{r}') + \Gamma_{xc}(\mathbf{r}, \mathbf{r}')$ [56–58]; $\pi(\mathbf{r}, \mathbf{r}')$ is normalized to the number of ordered pairs of distinct electrons, $N(N-1)$.

The theory briefly outlined above is based on an analysis of the distribution of the electron density $\rho(\mathbf{r})$ and the behavior of its gradient $\nabla\rho(\mathbf{r})$. Evidently, other scalar and vector fields may, in principle, be chosen for such an analysis, provided that the physical picture underlying the theoretical model is sufficiently clear. If an electron–nuclear system is characterized by a scalar potential field, such as the Slater total static potential $\varphi_{\mathrm{em}}(\mathbf{r})$ [59, 60]:

$$\varphi_{\mathrm{em}}(\mathbf{r}) = \frac{1}{\rho(\mathbf{r})} \int \frac{1}{|\mathbf{r}-\mathbf{r}'|} [-\rho(\mathbf{r}) \sum_n Z_n \delta(\mathbf{r}' - \mathbf{R}_n) + \pi(\mathbf{r}, \mathbf{r}')] \mathrm{d}\mathbf{r}' = \int \frac{1}{|\mathbf{r}-\mathbf{r}'|} [-\sum_n Z_n \delta(\mathbf{r}' - \mathbf{R}_n) + \rho(\mathbf{r}') + h_{xc}(\mathbf{r}, \mathbf{r}')] \mathrm{d}\mathbf{r}', \quad (5)$$

then a corresponding conservative force field—the Slater total static force field $\mathcal{F}(\mathbf{r}) = -\nabla\varphi_{\mathrm{em}}(\mathbf{r})$ [3, 4, 16, 27, 61, 62]—can naturally be associated with this potential:

$$\mathcal{F}(\mathbf{r}) = \int \frac{(\mathbf{r}-\mathbf{r}')}{|\mathbf{r}-\mathbf{r}'|^3} [-\sum_n Z_n \delta(\mathbf{r}' - \mathbf{R}_n) + \rho(\mathbf{r}') + h_{xc}(\mathbf{r}, \mathbf{r}')] \mathrm{d}\mathbf{r}' - \int \frac{1}{|\mathbf{r}-\mathbf{r}'|} \nabla_{\mathbf{r}} h_{xc}(\mathbf{r}, \mathbf{r}') \mathrm{d}\mathbf{r}'. \quad (6)$$

[2] It should be recognized that the use of a bond path as an indicator of chemical bonding or the presence of a chemical bond rests, to a considerable extent, on a postulate. Nevertheless, for equilibrium geometries, this criterion is defensible and useful, particularly given that (i) chemical bonding appears to encompass a complex interplay of distinct physical phenomena; (ii) the term itself lacks a precise operational definition; and (iii) the underlying concept stems from classical chemical notions rather than from the quantum-mechanical formalism, which provides no unique observable corresponding to a chemical bond.

Unless otherwise stated, atomic units are used throughout. Here, Z_n is the charge number of the nth atomic nucleus; $\mathbf{R}_n$ is the position vector of the nth nucleus; the exchange–correlation, or Fermi–Coulomb, hole density is defined as $h_{xc}(\mathbf{r},\mathbf{r}') = \Gamma_{xc}(\mathbf{r},\mathbf{r}')/\rho(\mathbf{r})$; and the integration variable $\mathbf{r}'$ ranges over all three-dimensional space, whereas the index n runs over all nuclei of the system.

The expressions in Eqs. (5) and (6) are written in terms of integrals over the distributions of all charged particles in the system, *i.e.*, nuclei and electrons [27, 28]. Alternatively, averaging the Coulomb interaction energy operator for electron i, $\hat{V}_i$, over the conditional probability distribution of the remaining $N-1$ electrons, given that electron i is at $\mathbf{r}$, yields the Slater total static potential $\varphi_{\mathrm{em}}(\mathbf{r})$, which represents the mean Coulomb interaction energy of that electron with all the other charged particles of the electron–nuclear system—its nuclei and remaining electrons. In other words, $\varphi_{\mathrm{em}}(\mathbf{r})$ is the electronic Coulomb potential density normalized by the electron density, provided that $\rho(\mathbf{r}) > 0$, and can therefore be expressed as a ratio of expectation values of local observable densities:

$$\varphi_{\mathrm{em}}(\mathbf{r}) = \frac{\left\langle \Psi \middle| \sum_{i=1}^{N} \delta(\mathbf{r}-\mathbf{r}_i)\, \hat{V}_i \middle| \Psi \right\rangle}{\left\langle \Psi \middle| \sum_{i=1}^{N} \delta(\mathbf{r}-\mathbf{r}_i) \middle| \Psi \right\rangle}, \tag{7}$$

where Ψ denotes the normalized N-electron wave function, and the Coulomb interaction energy operator for electron i, $\hat{V}_i$, comprises all terms in the potential-energy operator of the electronic Hamiltonian, $\hat{V}$, that describe interactions of electron i with the nuclei and the other electrons:

$$\hat{V}_i = -\sum_n \frac{Z_n}{|\mathbf{r}_i-\mathbf{R}_n|} + \sum_{\substack{j=1 \\ j\neq i}}^{N} \frac{1}{|\mathbf{r}_i-\mathbf{r}_j|}, \tag{8}$$

$$\hat{V} = -\sum_{i=1}^{N} \sum_n \frac{Z_n}{|\mathbf{r}_i-\mathbf{R}_n|} + \sum_{i<j}^{N} \frac{1}{|\mathbf{r}_i-\mathbf{r}_j|}. \tag{9}$$

Here, the indices i and j run over the N electrons. In both $\hat{V}$ and $\hat{V}_i$, the first term describes attractive electron–nuclear interactions and the second repulsive electron–electron interactions, with $\hat{V}$ accounting for all such interactions in the system and $\hat{V}_i$ only for those involving electron i. Although each operator counts every included pair of distinct electrons only once, summing $\hat{V}_i$ over all i counts each electron–electron interaction twice, once for each of the two electrons involved. The electronic Coulomb potential density corresponding to the numerator of Eq. (7) was previously discussed in

references [63, 64]. However, the notation in reference [64] does not explicitly distinguish the total electronic potential-energy operator $\hat{V}$ from the interaction operator for an individual electron, $\hat{V}_i$, although the explicit expression for the potential density corresponds to the latter. This distinction is drawn in reference [63] and, through the expression for $\hat{V}_i$ in Eq. (8), in the present formulation. Thus, an operator-based definition of $\varphi_{\mathrm{em}}(\mathbf{r})$ is established—a definition grounded directly in the formalism of quantum mechanics. This definition provides a rigorous basis for deriving the chemically significant physical quantities discussed or introduced below.

The potential itself is of particular importance to chemistry for the following reason. The value of $\varphi_{\mathrm{em}}(\mathbf{r})$ evaluated at the corresponding line-type saddle equilibrium point $\mathbf{r}_\pi$ of $\mathcal{F}(\mathbf{r})$, denoted $\varphi_{\mathrm{em}}(\mathbf{r}_\pi)$, represents the height of the internuclear potential barrier experienced by an electron [1, 3–5, 10, 65]: the lower $\varphi_{\mathrm{em}}(\mathbf{r}_\pi)$ is, the lower the potential barrier is and, consequently, the more readily two-center electron delocalization occurs.

Attention now turns from $\varphi_{\mathrm{em}}(\mathbf{r})$ to the associated conservative Slater total static force field $\mathcal{F}(\mathbf{r}) = -\nabla\varphi_{\mathrm{em}}(\mathbf{r})$, which gives the force acting on an electron at $\mathbf{r}$ in real space. The positions of the attractors of the force-field lines are expected to coincide with those of the atomic nuclei, whereas a zero-flux surface $P(\alpha|\omega)$ lies between the attractors α and ω. At each point of $P(\alpha|\omega)$, the force contributions arising from charges distributed in the regions on either side of the surface balance one another in the direction normal to the surface [4]:

$$\mathcal{F}(\mathbf{r}) \cdot \mathbf{n}(\mathbf{r}) = [\mathbf{F}_{\mathrm{es}}(\mathbf{r}) + \mathbf{F}_{xc}(\mathbf{r})] \cdot \mathbf{n}(\mathbf{r}) = 0, \qquad \forall \mathbf{r} \in P(\Omega_P). \tag{10}$$

More rigorously, the normal component of $\mathcal{F}(\mathbf{r})$ vanishes at every point on this surface. The physical content—namely, the nucleus and a portion of the electron cloud—enclosed within the basin Ω_P is defined here as an $\mathcal{F}$-pseudoatom. The P boundary acts as an *internal turning surface* for a charge source: to cross this surface, an electron must overcome the attraction exerted by the force field $\mathcal{F}(\mathbf{r})$ and directed toward the atomic nucleus or, equivalently, surmount a static potential barrier that reaches its locally highest values at the surface [4, 10].

Furthermore, analogous reasoning can be applied to the electrostatic potential $\varphi_{\mathrm{es}}(\mathbf{r})$ and the per-electron electrostatic force field $\mathbf{F}_{\mathrm{es}}(\mathbf{r}) = -\nabla[-\varphi_{\mathrm{es}}(\mathbf{r})]$ [1, 16, 27, 62]:

$$\varphi_{\mathrm{es}}(\mathbf{r}) = \left\langle \Psi \middle| \sum_n \frac{Z_n}{|\mathbf{r}-\mathbf{R}_n|} - \sum_{j=1}^{N} \frac{1}{|\mathbf{r}-\mathbf{r}_j|} \middle| \Psi \right\rangle = \int \frac{1}{|\mathbf{r}-\mathbf{r}'|} [\sum_n Z_n \delta(\mathbf{r}' - \mathbf{R}_n) - \rho(\mathbf{r}')] \mathrm{d}\mathbf{r}', \tag{11}$$

$$\mathbf{F}_{\mathrm{es}}(\mathbf{r}) = \left\langle \Psi \middle| -\sum_n Z_n \frac{(\mathbf{r}-\mathbf{R}_n)}{|\mathbf{r}-\mathbf{R}_n|^3} + \sum_{j=1}^{N} \frac{(\mathbf{r}-\mathbf{r}_j)}{|\mathbf{r}-\mathbf{r}_j|^3} \middle| \Psi \right\rangle = \int \frac{(\mathbf{r}-\mathbf{r}')}{|\mathbf{r}-\mathbf{r}'|^3} [-\sum_n Z_n \delta(\mathbf{r}' - \mathbf{R}_n) + \rho(\mathbf{r}')] \mathrm{d}\mathbf{r}'. \tag{12}$$

In this case, the zero-flux condition takes the following form:

$$\mathbf{F}_{\mathrm{es}}(\mathbf{r}) \cdot \mathbf{n}(\mathbf{r}) = 0, \qquad \forall \mathbf{r} \in U(\Omega_U). \tag{13}$$

The physical content enclosed within the basin Ω_U is defined here as an $\mathbf{F}_{\mathrm{es}}$-pseudoatom. In Eq. (7), $\mathbf{r}$ specifies the position of an electron of the system; the Coulomb interaction energy of that electron is averaged over the conditional distribution of the remaining $N-1$ electrons. In contrast, in Eqs. (11) and (12), $\mathbf{r}$ is a fixed observation point, and the electronic contributions to $\varphi_{\mathrm{es}}(\mathbf{r})$ and $\mathbf{F}_{\mathrm{es}}(\mathbf{r})$ are obtained by averaging over the positions of all N electrons, without conditioning on the presence of an electron at that point. Eq. (11) uniquely defines $\varphi_{\mathrm{es}}(\mathbf{r})$ from the physical charge distribution, with the zero of the potential fixed at infinity.

A comparison of the expressions for the aforementioned pair of force fields, $\mathcal{F}(\mathbf{r}) = \mathbf{F}_{\mathrm{es}}(\mathbf{r}) + \mathbf{F}_{xc}(\mathbf{r})$ and $\mathbf{F}_{\mathrm{es}}(\mathbf{r})$, *i.e.*, Eq. (6) *versus* Eq. (12), shows that all differences between them are directly determined by the Slater exchange–correlation force field $\mathbf{F}_{xc}(\mathbf{r}) = -\nabla\varphi_{xc}^{\mathrm{hole}}(\mathbf{r})$ [14, 16, 17, 19, 23, 24, 27]:

$$\mathbf{F}_{xc}(\mathbf{r}) = \int \frac{(\mathbf{r}-\mathbf{r}')}{|\mathbf{r}-\mathbf{r}'|^3} h_{xc}(\mathbf{r},\mathbf{r}') \mathrm{d}\mathbf{r}' - \int \frac{1}{|\mathbf{r}-\mathbf{r}'|} \nabla_{\mathbf{r}} h_{xc}(\mathbf{r},\mathbf{r}') \mathrm{d}\mathbf{r}'. \tag{14}$$

This conclusion is also formalized in the zero-flux condition for $\mathcal{F}(\mathbf{r})$ given by Eq. (10).

Importantly, force-field pseudoatoms of different types *reflect the state of a given real chemical atom* within the electron–nuclear system as a whole and should be regarded as *real-space-defined attributes of that atom*. A force-field path—a pair of trajectory lines in a given force field, both originating at the same saddle-type equilibrium point and each terminating at a distinct attractor, typically located at an atomic nucleus—is considered a *mechanically* grounded topological signature

of interattractor connectivity and *interatomic binding* [1, 5, 10, 12]. Within an internuclear region, such a binding path in $\mathcal{F}(\mathbf{r})$ can be viewed as the spine of a *real-space-defined channel for favorable electron sharing in which two-center electron delocalization is facilitated* [3], an interpretation supported by the lower values of $\varphi_{\mathrm{em}}(\mathbf{r})$ along the path relative to those at nearby points displaced laterally from it. We also highlight the distinction between chemical bonding and interatomic binding, with the latter understood in force-field terms, and emphasize the rigorous physical foundation and chemical significance of interatomic binding.

To overcome the difficulties inherent in interpreting vector fields, the use of the scalar projection of a partial force field onto the cumulative force field has been proposed [14, 19]. Examples include $[\mathbf{F}_{xc}(\mathbf{r}) \cdot \mathcal{F}(\mathbf{r})]/\|\mathcal{F}(\mathbf{r})\|$ and $[\mathbf{F}_{x}(\mathbf{r}) \cdot \mathcal{F}(\mathbf{r})]/\|\mathcal{F}(\mathbf{r})\|$, in which the Slater exchange–correlation force field $\mathbf{F}_{xc}(\mathbf{r})$ and the exchange-only force field $\mathbf{F}_{x}(\mathbf{r})$, respectively, serve as the partial force fields. The spatial distribution of the latter projection has been shown to distinguish domains associated with lone electron pairs from those associated with electron pairs in internuclear binding regions, thereby providing a means of differentiating these features of chemical structure in real space [14, 16, 17, 23].

The next step is to introduce the relevant charge densities. By Gauss's law (Maxwell's first equation) [14, 20, 27], the total static charge density $q_{\mathrm{em}}(\mathbf{r})$, which serves as the source charge distribution responsible for the generation of the force field $\mathcal{F}(\mathbf{r})$ [19, 20, 24, 27, 28, 66], can be straightforwardly expressed as

$$q_{\mathrm{em}}(\mathbf{r}) = \frac{1}{4\pi}\nabla \cdot \mathcal{F}(\mathbf{r}) = -\sum_n Z_n \delta(\mathbf{r} - \mathbf{R}_n) + \rho(\mathbf{r}) + q_{xc}(\mathbf{r}), \tag{15}$$

where the last summand [24, 27, 67, 68] is given by

$$q_{xc}(\mathbf{r}) = \frac{1}{4\pi}\nabla \cdot \mathbf{F}_{xc}(\mathbf{r}) = h_{xc}(\mathbf{r},\mathbf{r}) + \frac{1}{2\pi}\int \frac{(\mathbf{r}-\mathbf{r}')}{|\mathbf{r}-\mathbf{r}'|^3} \cdot \nabla_{\mathbf{r}} h_{xc}(\mathbf{r},\mathbf{r}')\,\mathrm{d}\mathbf{r}' - \frac{1}{4\pi}\int \frac{1}{|\mathbf{r}-\mathbf{r}'|}\nabla_{\mathbf{r}}^2 h_{xc}(\mathbf{r},\mathbf{r}')\mathrm{d}\mathbf{r}'. \tag{16}$$

In physical terms, Eq. (15) implies that $q_{\mathrm{em}}(\mathbf{r})$ is the effective charge density experienced by an electron in a many-electron system, whether mononuclear or multinuclear. Consequently, the Slater self-consistent electronic charge density $\rho(\mathbf{r}) + q_{xc}(\mathbf{r})$ represents the electronic component of

$q_{\mathrm{em}}(\mathbf{r})$: the electron density $\rho(\mathbf{r})$ reflects classical electron–electron repulsion and provides a measure of the accumulation of negative charge within the electron cloud; the Slater exchange–correlation charge density $q_{xc}(\mathbf{r})$ incorporates contributions arising from both Fermi correlation (sometimes called Pauli correlation)—which originates from the antisymmetry of the many-electron wave function and gives rise to same-spin electron avoidance—and Coulomb correlation—which originates from the effects of electron–electron repulsion not captured by a mean-field description that includes exchange, and which alters the probability distribution of interelectronic separations in a complex manner, generally reducing the probability of finding electrons at short separations while increasing it over certain ranges of larger separations—and provides, in turn, a real-space measure of how these electron correlations modify the *effective* electron–electron repulsion experienced by an electron at $\mathbf{r}$ [27].

Negative values of $q_{xc}(\mathbf{r})$ locally lower both $q_{\mathrm{em}}(\mathbf{r})$ and $\rho(\mathbf{r}) + q_{xc}(\mathbf{r})$, thereby indicating attenuation of this repulsion, and are interpreted as reflecting the *condensation of electron-pair density within the many-electron cloud*; positive values of $q_{xc}(\mathbf{r})$, by contrast, locally increase both quantities, thereby indicating enhancement of the effective repulsion, and are interpreted as reflecting the decondensation of that density in real space [14, 20, 21, 23, 24, 27]. The decomposition of $q_{xc}(\mathbf{r})$ into the terms on the right-hand side of Eq. (16) identifies the distinct contributions from the local, directional, and curvature-related features of $h_{xc}(\mathbf{r}, \mathbf{r}')$ and thereby reveals how nonlocal electron correlation shapes the condensation and decondensation of electron-pair density [24, 27]. Furthermore, one can formally distinguish between the exchange-only charge density $q_x(\mathbf{r})$ arising from Fermi–Pauli correlation and the correlation charge density $q_c(\mathbf{r})$ arising from Coulomb correlation. The former is directly associated with *electron-pair formation*, whereas the latter reflects *modifications* of this phenomenon that are likewise quantum-mechanical in nature. By construction, $q_{xc}(\mathbf{r}) = q_x(\mathbf{r}) + q_c(\mathbf{r})$. Understanding the role of Coulomb correlation effects in shaping the (de)condensation of electron-pair density is an important task that is addressed in part in the present article.

Three important points concerning the charge densities discussed here should be noted. First, the Gauss-type relation allows a bilocal representation of a charge density to be transformed into a corresponding local form; in particular, the Fermi–Coulomb hole density $h_{xc}(\mathbf{r},\mathbf{r}')$ and the conditional electron density $\pi(\mathbf{r},\mathbf{r}')/\rho(\mathbf{r}) = \rho(\mathbf{r}') + h_{xc}(\mathbf{r},\mathbf{r}')$ appearing in Eqs. (5) and (6) have the local counterparts $q_{xc}(\mathbf{r})$ and $\rho(\mathbf{r}) + q_{xc}(\mathbf{r})$, respectively [24, 27, 28]. Second, the first two of the three terms on the right-hand side of Eq. (15) are the physical charge components that constitute $-q_{\mathrm{es}}(\mathbf{r})$, whereas $q_{xc}(\mathbf{r})$ is an effective charge density that does not correspond to a physical electronic density but serves as the source of the force field $\mathbf{F}_{xc}(\mathbf{r})$ [14, 19, 20, 24, 27]. Third, $q_{xc}(\mathbf{r})$ compensates for electron self-interaction [19, 27].

With the potential taken to vanish at infinity, the free-space Green's function for the Poisson equation, $\nabla^2\varphi_{\mathrm{em}}(\mathbf{r}) = -4\pi q_{\mathrm{em}}(\mathbf{r})$, provides the basis for defining the local source of $\varphi_{\mathrm{em}}(\mathbf{r})$ as

$$\mathrm{LS}_{\varphi_{\mathrm{em}}}(\mathbf{r},\mathbf{r}') = -\frac{1}{4\pi}\frac{\nabla_{\mathbf{r}'}^2\,\varphi_{\mathrm{em}}(\mathbf{r}')}{|\mathbf{r}-\mathbf{r}'|} = \frac{q_{\mathrm{em}}(\mathbf{r}')}{|\mathbf{r}-\mathbf{r}'|}. \tag{17}$$

This function describes the contribution per unit source volume at $\mathbf{r}'$ to the potential $\varphi_{\mathrm{em}}(\mathbf{r})$ at the reference point $\mathbf{r}$. Integration of $\mathrm{LS}_{\varphi_{\mathrm{em}}}(\mathbf{r},\mathbf{r}')$ over an atomic basin Ω_S enclosing a single nucleus of charge number Z at $\mathbf{R}$ yields the corresponding source function:

$$\mathrm{SF}_{\varphi_{\mathrm{em}}}(\mathbf{r},\Omega_S) = \int_{\Omega_S}\frac{q_{\mathrm{em}}(\mathbf{r}')}{|\mathbf{r}-\mathbf{r}'|}\,\mathrm{d}\mathbf{r}' = -\frac{Z}{|\mathbf{r}-\mathbf{R}|} + \int_{\Omega_S}\frac{\rho(\mathbf{r}')+q_{xc}(\mathbf{r}')}{|\mathbf{r}-\mathbf{r}'|}\,\mathrm{d}\mathbf{r}'. \tag{18}$$

The first integral in Eq. (18) quantifies the contribution of the corresponding atom to the total static potential $\varphi_{\mathrm{em}}(\mathbf{r})$; the second gives that atom's contribution to the electron–electron interaction potential $\varphi_{\mathrm{ee}}(\mathbf{r})$. For quantum-chemical analysis [*e.g.*, in assessing electrophilicity; see reference [26] on its relation to $\varphi_{\mathrm{em}}(\mathbf{r})$], each atomic contribution can also be expressed as a signed percentage of the corresponding potential, provided that its value at $\mathbf{r}$ is finite and nonzero. Furthermore, rewriting Eq. (18) in terms of the electrostatic source function $\mathrm{SF}_{\varphi_{\mathrm{es}}}(\mathbf{r},\Omega_S)$ [69, 70] isolates the nonclassical exchange–correlation component $\mathrm{SF}_{\varphi_{xc}^{\mathrm{hole}}}(\mathbf{r},\Omega_S)$:

$$\mathrm{SF}_{\varphi_{\mathrm{em}}}(\mathbf{r},\Omega_S) = -\mathrm{SF}_{\varphi_{\mathrm{es}}}(\mathbf{r},\Omega_S) + \mathrm{SF}_{\varphi_{xc}^{\mathrm{hole}}}(\mathbf{r},\Omega_S) = -\mathrm{SF}_{\varphi_{\mathrm{es}}}(\mathbf{r},\Omega_S) + \int_{\Omega_S}\frac{q_{xc}(\mathbf{r}')}{|\mathbf{r}-\mathbf{r}'|}\,\mathrm{d}\mathbf{r}'. \tag{19}$$

Equations (18) and (19) also apply to pseudoatomic basins, with Ω_S replaced by the corresponding integration domain. For basins containing no nucleus, the nuclear term in Eq. (18) is absent. The expressions above employ the Coulomb kernel appropriate to isolated systems (including atomic or molecular clusters large enough to represent the local environment within a crystal [28]); for charge-neutral periodic crystals, the same source-function formalism can be extended by replacing this kernel with the zero-mean periodic Coulomb kernel, thereby reconstructing $\varphi_{\mathrm{em}}(\mathbf{r})$ relative to its unit-cell average.

By conceptual analogy with the atoms-in-molecules requirement expressed by Eq. (2), charge constraints [16, 19, 20, 27] that determine the charges of an $\mathcal{F}$-pseudoatom, $Q_{\mathcal{F}} = Z - \iiint_{\Omega_P} \rho(\mathbf{r})\mathrm{d}\Omega_P$, and of an $\mathbf{F}_{\mathrm{es}}$-pseudoatom, $Q_{\mathbf{F}_{\mathrm{es}}} = Z - \iiint_{\Omega_U} \rho(\mathbf{r})\mathrm{d}\Omega_U$, can be derived:

$$Z - \iiint_{\Omega_P} \rho(\mathbf{r})\mathrm{d}\Omega_P = \iiint_{\Omega_P} q_{xc}(\mathbf{r})\mathrm{d}\Omega_P + \frac{\sigma_P}{4\pi}\left[\sum_n Z_n - N + 1\right], \tag{20}$$

$$Z - \iiint_{\Omega_U} \rho(\mathbf{r})\mathrm{d}\Omega_U = \frac{\sigma_U}{4\pi}\left[\sum_n Z_n - N\right], \tag{21}$$

respectively. Equations (20) and (21) impose constraints on the partitioning and spatial distribution of effective and physical charge in an electron–nuclear system, respectively [16, 27]. In this sense, these charge constraints shape the electron cloud. Here, σ_P and σ_U represent the solid angles subtended by the intersections of the respective basins Ω_P and Ω_U with the enveloping sphere about the system's center of charge, and N denotes the total number of electrons in the system.

Within density functional theory (DFT), Eq. (20) retains its form when the response-potential contribution is included in the nonclassical terms of both the static force field and the associated charge density, provided that the Ω_P basins are defined by the resulting total static force field [20]. This follows because, under the usual asymptotic conditions for an isolated finite system, the screening potential $\varphi_{xc}^{\mathrm{hole}}(\mathbf{r})$ supplies the leading $-1/r$ term of the DFT exchange–correlation potential $\varphi_{xc}(\mathbf{r}) = \varphi_{xc}^{\mathrm{hole}}(\mathbf{r}) + \varphi_{xc}^{\mathrm{resp}}(\mathbf{r})$, while the response potential $\varphi_{xc}^{\mathrm{resp}}(\mathbf{r})$ decays more rapidly [27, 71]; accordingly, in the DFT exchange–correlation force field $-\nabla\varphi_{xc}(\mathbf{r})$, the radial component of the screening contribution $\mathbf{F}_{xc}(\mathbf{r}) = -\nabla\varphi_{xc}^{\mathrm{hole}}(\mathbf{r})$ is asymptotic to $-1/r^2$, whereas that of the

response contribution $-\nabla\varphi_{xc}^{\mathrm{resp}}(\mathbf{r})$ decays faster than $1/r^2$ and therefore yields no flux at infinity for an open Ω_P basin, leaving the coefficient of σ_P unchanged. Note that, in the spin-unpolarized case, the DFT total static potential and its associated force field take their Slater forms if the response term is omitted [24]. In a stationary electronic ground state,[3] the von Weizsäcker and Pauli components of the DFT total kinetic force field together balance the DFT total static force field at every point where the fields are defined. As a consequence of this pointwise balance, the DFT form of Eq. (20) has a kinetic counterpart: the von Weizsäcker and Pauli charges within each Ω_P basin sum to the negative of its total static charge [20].

According to the Ostrogradsky–Gauss divergence theorem for an unbounded domain [27], a nonzero charge of an $\mathcal{F}$-pseudoatom implies a nonzero flux of $\mathbf{F}_{\mathrm{es}}(\mathbf{r})$ through the pseudoatomic boundary P and, consequently, a corresponding law-governed spatial separation of the two zero-flux surfaces P and U [16, 19, 27]:

$$Q_{\mathcal{F}} = Z - \iiint_{\Omega_P} \rho(\mathbf{r})\mathrm{d}\Omega_P = -\frac{1}{4\pi}\iint_P [\mathbf{F}_{\mathrm{es}}(\mathbf{r})\cdot\mathbf{n}(\mathbf{r})]\mathrm{d}P + \frac{\sigma_P}{4\pi}[\textstyle\sum_n Z_n - N]. \tag{22}$$

Importantly, Ω_P*-partitioning ensures charge separation and prevents electron sharing between adjoining force-field basins* [19, 20, 27]. At the same time, the magnitudes of $Q_{\mathcal{F}}$ are generally smaller than those of $Q_{\nabla\rho}$, and the differences between these charges vary in the expected manner with the nature of the interactions in the immediate environment of the atom in question [3, 7, 10–12, 20, 27, 72–75]. From this perspective, the $\mathcal{F}$-pseudoatomic charge $Q_{\mathcal{F}}$ may be interpreted as the ionic (noncovalent) component of the corresponding atomic charge $Q_{\nabla\rho}$ [10–12, 15, 16, 20, 22]. This statement is also supported by the data presented below in the "Results and discussion" section.

The presence of an electrostatic charge $Q_{\nabla\rho}$ on an atom [see Eq. (3)] likewise implies a flux of $\mathbf{F}_{\mathrm{es}}(\mathbf{r})$ through the boundary surface S [27, 76]:

$$Q_{\nabla\rho} = Z - \iiint_{\Omega_S} \rho(\mathbf{r})\mathrm{d}\Omega_S = -\frac{1}{4\pi}\iint_S [\mathbf{F}_{\mathrm{es}}(\mathbf{r})\cdot\mathbf{n}(\mathbf{r})]\mathrm{d}S + \frac{\sigma_S}{4\pi}[\textstyle\sum_n Z_n - N], \tag{23}$$

[3] In some earlier studies, the term "equilibrium" was used in this context to denote electronic stationarity in the ground state, without necessarily implying mechanical equilibrium of the nuclei.

where σ_S is the solid angle subtended by the intersection of the specified atomic basin Ω_S with the enveloping sphere constructed around the system's center of charge. This line of reasoning can be taken further by introducing the total effective atomic charge $Q_{\nabla\rho}^{\mathrm{eff}/\mathcal{F}}$ [28], defined here in terms of the flux of $\mathcal{F}(\mathbf{r})$ across the same boundary surface S:

$$Q_{\nabla\rho}^{\mathrm{eff}/\mathcal{F}} = Z - \iiint_{\Omega_S}[\rho(\mathbf{r}) + q_{xc}(\mathbf{r})]\mathrm{d}\Omega_S = -\frac{1}{4\pi}\iint_S[\mathcal{F}(\mathbf{r})\cdot\mathbf{n}(\mathbf{r})]\mathrm{d}S + \frac{\sigma_S}{4\pi}[\textstyle\sum_n Z_n - N + 1]. \qquad (24)$$

Thus, each atomic charge, whether physical (electrostatic) or effective, uniquely determines the flux of the corresponding force field through the atomic boundary surface S, and *vice versa*.

Considering the fluxes of $\mathbf{F}_{\mathrm{es}}(\mathbf{r})$ and $\mathcal{F}(\mathbf{r})$ through the individual interatomic surfaces $S(\alpha|\omega)$, which together constitute the entire atomic boundary surface S, makes it possible to distinguish the contribution—and, in some cases, even several components of this contribution—of each polar $\omega\alpha$ interaction to the interatomic transfer of the physical electronic charge and that of the effective self-consistent electronic charge, as well as to the resulting atomic charges $Q_{\nabla\rho}$ and $Q_{\nabla\rho}^{\mathrm{eff}/\mathcal{F}}$ [19, 27]:

$$\frac{1}{4\pi}\iint_{S(\alpha|\omega)}[\mathbf{F}_{\mathrm{es}}(\mathbf{r})\cdot\mathbf{n}(\mathbf{r})]\mathrm{d}S(\alpha|\omega) - \frac{\sigma_\cap}{4\pi}[\textstyle\sum_n Z_n - N] = \iiint_{(\Omega_S^\alpha\cap\Omega_U^\omega)}\rho(\mathbf{r})\mathrm{d}(\Omega_S^\alpha\cap\Omega_U^\omega), \qquad (25)$$

$$\frac{1}{4\pi}\iint_{S(\alpha|\omega)}[\mathcal{F}(\mathbf{r})\cdot\mathbf{n}(\mathbf{r})]\mathrm{d}S(\alpha|\omega) - \frac{\sigma_\cap}{4\pi}[\textstyle\sum_n Z_n - N + 1] = \iiint_{(\Omega_S^\alpha\cap\Omega_P^\omega)}[\rho(\mathbf{r}) + q_{xc}(\mathbf{r})]\mathrm{d}(\Omega_S^\alpha\cap\Omega_P^\omega), \qquad (26)$$

where $\sigma_\cap$ denotes the solid angle subtended by the intersection of the corresponding open interbasin region with the enveloping sphere. The Greek letters ω and α denote the nuclei of the electron-donor and electron-acceptor atoms, respectively, and the same labels are assigned to the force-field basins whose attractors coincide with the corresponding nuclear positions. The occurrence of interbasin intersections of the $\Omega_S^\alpha\cap\Omega_U^\omega$ and $\Omega_S^\alpha\cap\Omega_P^\omega$ types is a direct consequence of *interatomic charge-transfer phenomena* that lead to the redistribution of physical and effective charges [27]. In particular, the charge $\iiint_{(\Omega_S^\alpha\cap\Omega_U^\omega)}\rho(\mathbf{r})\mathrm{d}(\Omega_S^\alpha\cap\Omega_U^\omega)$ quantifies $\omega\rightarrow\alpha$ *interatomic electron transfer*[4] [1, 3, 4, 6,

[4] The concept of charge transfer (or electron transfer), as defined in the present work, should be distinguished from that of electron transport.

16, 18, 19, 23, 26], whereas the charge $\iiint_{(\Omega_S^\alpha \cap \Omega_P^\omega)} \rho(\mathbf{r})\mathrm{d}(\Omega_S^\alpha \cap \Omega_P^\omega)$ serves as a quantitative descriptor of *quantum chemical response*[5] induced by $\omega \to \alpha$ interatomic electron transfer and may be interpreted as the shared (covalent) part of the electronic charge transferred interatomically [3–5, 11, 12, 16, 17, 19, 20]. In this context, it is appropriate to recall that the electron-transfer-induced quantum chemical response is a physical phenomenon reflecting the natural ability of interacting atoms to retain relatively small—or, in the limiting case, zero—$\mathcal{F}$-pseudoatomic charges despite atomic charging [3, 27]. The superposition of trajectory maps of the vector fields $\nabla\rho(\mathbf{r})$, $\mathbf{F}_{\mathrm{es}}(\mathbf{r})$, and $\mathcal{F}(\mathbf{r})$ has proved to be an excellent tool for identifying and describing the $\Omega_S^\alpha \cap \Omega_U^\omega$ and $\Omega_S^\alpha \cap \Omega_P^\omega$ interbasin intersections and for qualitatively analyzing charge redistribution among atoms [1]. In fact, such a superposition reflects the mechanical equilibrium established among force-field pseudoatoms of the same type in molecules and other many-electron multinuclear systems. Accordingly, interpreting the relative positions of the boundaries $S(\alpha|\omega)$, $U(\alpha|\omega)$, and $P(\alpha|\omega)$ as a descriptor of the participants in a Lewis acid–base interaction rather than as a reflection of charge redistribution appears physically untenable [4, 7, 10, 18, 22, 26].

Equations (25) and (26), together with the aforementioned superposition approach, constitute, in essence, a fruitful attempt at a unified treatment of the quantum theory of atoms in molecules and the force-field perspective on chemical structure. This integration gives rise to a new research direction—the pseudoatoms-in-molecules theoretical framework,[6] which is being actively developed

[5] The term "quantum chemical response" reflects both the origin and the chemical significance of the phenomenon. "Quantum" refers to its origin in electron correlation; "chemical" reflects its induction by interatomic electron transfer and, in systems containing two or more electrons, the fundamental role of this correlation—primarily Fermi–Pauli exchange correlation—in interatomic interactions, chemical bond covalency, and, more generally, chemical structure and its transformation. In the view of the present authors, this phenomenon deserves recognition commensurate with its exceptional importance to chemistry.

[6] The framework of "pseudoatoms in molecules," introduced and further developed by the present authors, takes its name from Bader's "atoms in molecules." The analogy is substantive: the relative arrangement and intersections of force-field and atomic basins provide a basis for interpreting differences between the corresponding spatial partitionings in terms of interatomic charge transfer and atomic charging. This

by the present authors [1, 3–5, 11, 16, 19, 20, 27]. To extend this framework, the atomic Slater force $\mathcal{F}(\Omega_S)$ may be introduced as a novel descriptor:

$$\mathcal{F}(\Omega_S) = \iiint_{\Omega_S} \mathcal{F}(\mathbf{r})\rho(\mathbf{r})\mathrm{d}\Omega_S. \tag{27}$$

This quantity is analogous to the atomic Ehrenfest force $\mathfrak{F}(\Omega_S) = \iiint_{\Omega_S} \mathfrak{F}(\mathbf{r})\mathrm{d}\Omega_S$ [39, 41, 77–80], where $\mathfrak{F}(\mathbf{r}) = \left\langle \Psi \middle| \sum_{i=1}^{N} \delta(\mathbf{r}-\mathbf{r}_i)\, \widehat{\mathfrak{F}}_i \middle| \Psi \right\rangle$ is the Ehrenfest force density field. Here, the force operator for electron i is defined by $\widehat{\mathfrak{F}}_i = -\nabla_i \hat{V} = -\nabla_i \hat{V}_i$.[7] The atomic force $\mathcal{F}(\Omega_S)$ can be represented as the sum of two vector contributions, both acting on a portion of the electron cloud within the atomic basin Ω_S of a many-electron multinuclear system: the contribution from the attractive electron–nuclear interaction, *i.e.*, $\iiint_{\Omega_S} \mathbf{F}_{\mathrm{ne}}(\mathbf{r})\rho(\mathbf{r})\mathrm{d}\Omega_S$, and the contribution from the repulsive electron–electron interaction, *i.e.*, $\iiint_{\Omega_S} \mathbf{F}_{\mathrm{ee}}(\mathbf{r})\rho(\mathbf{r})\mathrm{d}\Omega_S$; the latter, in turn, consists of the classical Hartree component, $\iiint_{\Omega_S} \mathbf{F}_{\mathrm{H}}(\mathbf{r})\rho(\mathbf{r})\mathrm{d}\Omega_S$, and the nonclassical Fermi–Coulomb component, $\iiint_{\Omega_S} \mathbf{F}_{xc}(\mathbf{r})\rho(\mathbf{r})\mathrm{d}\Omega_S$:

$$\mathcal{F}(\Omega_S) = \iiint_{\Omega_S} \mathbf{F}_{\mathrm{ne}}(\mathbf{r})\rho(\mathbf{r})\mathrm{d}\Omega_S + \iiint_{\Omega_S} \mathbf{F}_{\mathrm{ee}}(\mathbf{r})\rho(\mathbf{r})\mathrm{d}\Omega_S = \iiint_{\Omega_S} \mathbf{F}_{\mathrm{es}}(\mathbf{r})\rho(\mathbf{r})\mathrm{d}\Omega_S +$$

$$\iiint_{\Omega_S} \mathbf{F}_{xc}(\mathbf{r})\rho(\mathbf{r})\mathrm{d}\Omega_S = \iiint_{\Omega_S} \mathbf{F}_{\mathrm{ne}}(\mathbf{r})\rho(\mathbf{r})\mathrm{d}\Omega_S + \iiint_{\Omega_S} \mathbf{F}_{\mathrm{H}}(\mathbf{r})\rho(\mathbf{r})\mathrm{d}\Omega_S + \iiint_{\Omega_S} \mathbf{F}_{xc}(\mathbf{r})\rho(\mathbf{r})\mathrm{d}\Omega_S, \tag{28}$$

where the electron–nuclear interaction force field $\mathbf{F}_{\mathrm{ne}}(\mathbf{r})$, the electron–electron interaction force field $\mathbf{F}_{\mathrm{ee}}(\mathbf{r}) = -\nabla\varphi_{\mathrm{ee}}(\mathbf{r})$ [14, 17, 19, 27], and the Hartree force field $\mathbf{F}_{\mathrm{H}}(\mathbf{r})$ are expressed by

$$\mathbf{F}_{\mathrm{ne}}(\mathbf{r}) = \int \frac{(\mathbf{r}-\mathbf{r}')}{|\mathbf{r}-\mathbf{r}'|^3}[-\textstyle\sum_n Z_n \delta(\mathbf{r}'-\mathbf{R}_n)]\mathrm{d}\mathbf{r}', \tag{29}$$

$$\mathbf{F}_{\mathrm{ee}}(\mathbf{r}) = \int \frac{(\mathbf{r}-\mathbf{r}')}{|\mathbf{r}-\mathbf{r}'|^3}[\rho(\mathbf{r}') + h_{xc}(\mathbf{r},\mathbf{r}')]\mathrm{d}\mathbf{r}' - \int \frac{1}{|\mathbf{r}-\mathbf{r}'|}\nabla_{\mathbf{r}} h_{xc}(\mathbf{r},\mathbf{r}')\mathrm{d}\mathbf{r}', \tag{30}$$

$$\mathbf{F}_{\mathrm{H}}(\mathbf{r}) = \int \frac{(\mathbf{r}-\mathbf{r}')}{|\mathbf{r}-\mathbf{r}'|^3}\rho(\mathbf{r}')\mathrm{d}\mathbf{r}'. \tag{31}$$

---

perspective places charge redistribution at the center of the analysis of interatomic interactions in molecules, crystals, and other many-electron multinuclear systems.

[7] Although the family of operators, $\{\hat{V}_i\}_{i=1}^{N}$, does not form an additive decomposition of $\hat{V}$ for $N > 1$ (*vide supra*), the equality $\nabla_i \hat{V} = \nabla_i \hat{V}_i$ holds because $\hat{V} - \hat{V}_i$ contains only terms describing interactions of the remaining electrons with the nuclei and with one another; these terms are independent of $\mathbf{r}_i$ and therefore vanish upon differentiation with respect to $\mathbf{r}_i$.

The force decomposition in Eq. (28) enables a detailed analysis of the contributions of classical effects and quantum-mechanical Fermi–Coulomb correlation effects to the net atomic force, as well as of their relative significance. It should be noted that, for a given chemically bound atom, the difference between the total Slater force $\mathcal{F}(\Omega_S)$ and the total Ehrenfest force $\mathfrak{F}(\Omega_S)$ is given by

$$\mathcal{F}(\Omega_S) - \mathfrak{F}(\Omega_S) = \iiint_{\Omega_S} \mathbf{F}_{xc}^{\nabla h}(\mathbf{r})\rho(\mathbf{r})\mathrm{d}\Omega_S, \tag{32}$$

where $\mathbf{F}_{xc}^{\nabla h}(\mathbf{r}) = -\int \frac{1}{|\mathbf{r}-\mathbf{r}'|}\nabla_{\mathbf{r}} h_{xc}(\mathbf{r},\mathbf{r}')\mathrm{d}\mathbf{r}'$ is the last term in each of Eqs. (6), (14), and (30) and arises from the explicit dependence of $h_{xc}(\mathbf{r},\mathbf{r}')$ on the reference-electron position $\mathbf{r}$ [27]. An important avenue for future research would also be to investigate the properties of the pseudoatomic Slater force $\mathcal{F}(\Omega_P) = \iiint_{\Omega_P} \mathcal{F}(\mathbf{r})\rho(\mathbf{r})\mathrm{d}\Omega_P$ and the pseudoatomic Ehrenfest force $\mathfrak{F}(\Omega_E) = \iiint_{\Omega_E} \mathfrak{F}(\mathbf{r})\mathrm{d}\Omega_E$, as well as those of their components. The integration domains Ω_P and Ω_E are defined by the natural partitionings of real space provided by $\mathcal{F}(\mathbf{r})$ and $\mathfrak{F}(\mathbf{r})$, respectively.

Theoretical framework

This section uses the local variation of the Slater total static force field $\mathcal{F}(\mathbf{r})$ along the principal axes of the potential Hessian $H_{\varphi_{\mathrm{em}}}(\mathbf{r})$ to decompose the associated charge density $q_{\mathrm{em}}(\mathbf{r})$ into three directional contributions. Consider $\mathcal{F}(\mathbf{r}) = F_x(\mathbf{r})\hat{\mathbf{e}}_x + F_y(\mathbf{r})\hat{\mathbf{e}}_y + F_z(\mathbf{r})\hat{\mathbf{e}}_z$, which is defined on the three-dimensional Euclidean space $\mathbb{R}^3$ and expressed in a fixed orthonormal Cartesian basis $\{\hat{\mathbf{e}}_x, \hat{\mathbf{e}}_y, \hat{\mathbf{e}}_z\}$, with $\mathbf{r} = x\hat{\mathbf{e}}_x + y\hat{\mathbf{e}}_y + z\hat{\mathbf{e}}_z$. Here, $F_x(\mathbf{r})$, $F_y(\mathbf{r})$, and $F_z(\mathbf{r})$ are the scalar components of the vector field $\mathcal{F}(\mathbf{r})$ along the Cartesian x, y, and z axes, respectively. Moreover, the conservative nature of $\mathcal{F}(\mathbf{r}) = -\nabla\varphi_{\mathrm{em}}(\mathbf{r})$ allows these scalar components to be expressed as derivatives of the associated Slater total static potential $\varphi_{\mathrm{em}}(\mathbf{r})$. For the x component, $F_x(\mathbf{r}) = -\partial\varphi_{\mathrm{em}}(\mathbf{r})/\partial x$ and $\partial F_x(\mathbf{r})/\partial x = -\partial^2\varphi_{\mathrm{em}}(\mathbf{r})/\partial x^2$; the analogous identities are obtained by replacing x, in turn, by y and z. With this notation, the divergence of $\mathcal{F}(\mathbf{r})$ can be written in either of two forms. In terms of first-order partial derivatives of the scalar Cartesian components of $\mathcal{F}(\mathbf{r})$, it is

$$\nabla\cdot\mathcal{F}(\mathbf{r}) = \frac{\partial F_x(\mathbf{r})}{\partial x} + \frac{\partial F_y(\mathbf{r})}{\partial y} + \frac{\partial F_z(\mathbf{r})}{\partial z}. \tag{33}$$

Equivalently, in terms of second-order partial derivatives of $\varphi_{\mathrm{em}}(\mathbf{r})$, it is

$$\nabla \cdot \mathcal{F}(\mathbf{r}) = -\operatorname{tr} H_{\varphi_{\mathrm{em}}}(\mathbf{r}) = -\left[\frac{\partial^2 \varphi_{\mathrm{em}}(\mathbf{r})}{\partial x^2} + \frac{\partial^2 \varphi_{\mathrm{em}}(\mathbf{r})}{\partial y^2} + \frac{\partial^2 \varphi_{\mathrm{em}}(\mathbf{r})}{\partial z^2}\right]. \tag{34}$$

Here, tr denotes the trace operation. Each term on the right-hand side of Eq. (33) describes the local variation of the corresponding scalar Cartesian component of $\mathcal{F}(\mathbf{r})$. The individual terms on the right-hand side of Eq. (34) are the negatives of the Cartesian directional curvatures of $\varphi_{\mathrm{em}}(\mathbf{r})$, *i.e.*, the negatives of the diagonal elements of its Hessian, which is denoted by $H_{\varphi_{\mathrm{em}}}(\mathbf{r})$:

$$H_{\varphi_{\mathrm{em}}}(\mathbf{r}) = \begin{pmatrix} \frac{\partial^2 \varphi_{\mathrm{em}}(\mathbf{r})}{\partial x^2} & \frac{\partial^2 \varphi_{\mathrm{em}}(\mathbf{r})}{\partial x \partial y} & \frac{\partial^2 \varphi_{\mathrm{em}}(\mathbf{r})}{\partial x \partial z} \\ \frac{\partial^2 \varphi_{\mathrm{em}}(\mathbf{r})}{\partial y \partial x} & \frac{\partial^2 \varphi_{\mathrm{em}}(\mathbf{r})}{\partial y^2} & \frac{\partial^2 \varphi_{\mathrm{em}}(\mathbf{r})}{\partial y \partial z} \\ \frac{\partial^2 \varphi_{\mathrm{em}}(\mathbf{r})}{\partial z \partial x} & \frac{\partial^2 \varphi_{\mathrm{em}}(\mathbf{r})}{\partial z \partial y} & \frac{\partial^2 \varphi_{\mathrm{em}}(\mathbf{r})}{\partial z^2} \end{pmatrix}. \tag{35}$$

Because the Slater total charge density $q_{\mathrm{em}}(\mathbf{r})$ is defined by the Gauss-type relation $q_{\mathrm{em}}(\mathbf{r}) = \frac{1}{4\pi} \nabla \cdot \mathcal{F}(\mathbf{r})$ [see Eq. (15)], substituting the two expressions for $\nabla \cdot \mathcal{F}(\mathbf{r})$ from Eqs. (33) and (34) into this definition immediately gives

$$q_{\mathrm{em}}(\mathbf{r}) = \frac{1}{4\pi}\left[\frac{\partial F_x(\mathbf{r})}{\partial x} + \frac{\partial F_y(\mathbf{r})}{\partial y} + \frac{\partial F_z(\mathbf{r})}{\partial z}\right] \tag{36}$$

and

$$q_{\mathrm{em}}(\mathbf{r}) = -\frac{1}{4\pi} \operatorname{tr} H_{\varphi_{\mathrm{em}}}(\mathbf{r}) = -\frac{1}{4\pi}\left[\frac{\partial^2 \varphi_{\mathrm{em}}(\mathbf{r})}{\partial x^2} + \frac{\partial^2 \varphi_{\mathrm{em}}(\mathbf{r})}{\partial y^2} + \frac{\partial^2 \varphi_{\mathrm{em}}(\mathbf{r})}{\partial z^2}\right], \tag{37}$$

respectively. Each of the three terms on the right-hand side of Eq. (36) is a source- or sink-like directional contribution to $q_{\mathrm{em}}(\mathbf{r})$, corresponding to the local net outward flux per unit volume through the pair of infinitesimal faces normal to the corresponding Cartesian direction, as determined by the variation of the scalar component of $\mathcal{F}(\mathbf{r})$ along that direction. For a given contribution, positive values indicate source-like behavior of the relevant component—$F_x(\mathbf{r})$, $F_y(\mathbf{r})$, or $F_z(\mathbf{r})$, as appropriate—whereas negative values indicate sink-like behavior. In the representation given by Eq. (37), these same three directional contributions are expressed term by term as scalar contributions to $q_{\mathrm{em}}(\mathbf{r})$, each determined by the curvature of $\varphi_{\mathrm{em}}(\mathbf{r})$ along the same coordinate direction.

Since the trace of the Hessian is invariant under orthogonal transformations of the coordinate system, Eq. (37) can finally be rewritten in the local principal-axis frame of $H_{\varphi_{\mathrm{em}}}(\mathbf{r})$:

$$q_{\mathrm{em}}(\mathbf{r}) = -\frac{1}{4\pi}\,\mathrm{tr}\,H_{\varphi_{\mathrm{em}}}(\mathbf{r}) = -\frac{1}{4\pi}[\Lambda_1(\mathbf{r}) + \Lambda_2(\mathbf{r}) + \Lambda_3(\mathbf{r})]. \tag{38}$$

In this frame, the matrix $H_{\varphi_{\mathrm{em}}}(\mathbf{r})$ is diagonal, and its diagonal elements are the eigenvalues $\Lambda_1(\mathbf{r})$, $\Lambda_2(\mathbf{r})$, and $\Lambda_3(\mathbf{r})$, ordered as $\Lambda_1(\mathbf{r}) \leq \Lambda_2(\mathbf{r}) \leq \Lambda_3(\mathbf{r})$:

$$H_{\varphi_{\mathrm{em}}}(\mathbf{r}) = \begin{pmatrix} \Lambda_1(\mathbf{r}) & 0 & 0 \\ 0 & \Lambda_2(\mathbf{r}) & 0 \\ 0 & 0 & \Lambda_3(\mathbf{r}) \end{pmatrix}. \tag{39}$$

Accordingly, a negative eigenvalue of $H_{\varphi_{\mathrm{em}}}(\mathbf{r})$ corresponds to a *tensile principal mode of the local linear variation of the scalar Cartesian components* of $\mathcal{F}(\mathbf{r})$, whereas a positive eigenvalue corresponds to a *compressive principal mode* of the same variation, in each case along the corresponding principal direction.

In the present study, the characterization of chemical bonds is restricted to the eigenvalues of $H_{\varphi_{\mathrm{em}}}(\mathbf{r})$ evaluated at those Lagrange points $\mathbf{r}_\pi$ of $\mathcal{F}(\mathbf{r})$ that are the (3, +1) critical points of $\varphi_{\mathrm{em}}(\mathbf{r})$, or equivalently, the saddle-type equilibrium points of $\mathcal{F}(\mathbf{r})$. For practical purposes, $\Lambda_1(\mathbf{r}_\pi)$ characterizes the direction along the internuclear axis, whereas $\Lambda_2(\mathbf{r}_\pi)$ and $\Lambda_3(\mathbf{r}_\pi)$ characterize the directions perpendicular to this axis. For this local Hessian signature of +1, *i.e.*, $\Lambda_1(\mathbf{r}_\pi) < 0 < \Lambda_2(\mathbf{r}_\pi) \leq \Lambda_3(\mathbf{r}_\pi)$, the principal mode associated with $\Lambda_1(\mathbf{r}_\pi)$ represents the tensile, source-like contribution to $q_{\mathrm{em}}(\mathbf{r}_\pi)$, whereas the principal modes associated with $\Lambda_2(\mathbf{r}_\pi)$ and $\Lambda_3(\mathbf{r}_\pi)$ represent the two compressive, sink-like contributions. In fact, $\Lambda_1(\mathbf{r}_\pi)$, $\Lambda_2(\mathbf{r}_\pi)$, and $\Lambda_3(\mathbf{r}_\pi)$ are mechanical descriptors of the interatomic binding indicated by an internuclear path in the force field $\mathcal{F}(\mathbf{r})$ (see the "Theoretical background" section). Furthermore, for a given interatomic interaction, the quantity $\Xi(\mathbf{r}_\pi)$ is defined as the ratio of the absolute value of the tensile-mode eigenvalue, $|\Lambda_1(\mathbf{r}_\pi)|$, to the average of the two compressive-mode eigenvalues $\Lambda_2(\mathbf{r}_\pi)$ and $\Lambda_3(\mathbf{r}_\pi)$:

$$\Xi(\mathbf{r}_\pi) = \frac{2|\Lambda_1(\mathbf{r}_\pi)|}{\Lambda_2(\mathbf{r}_\pi)+\Lambda_3(\mathbf{r}_\pi)}. \tag{40}$$

Note that the eigenvalues $\Lambda_1(\mathbf{r}_\pi)$, $\Lambda_2(\mathbf{r}_\pi)$, and $\Lambda_3(\mathbf{r}_\pi)$ were previously considered in references [1, 61]. A quantity similar to $\Xi(\mathbf{r}_\pi)$ but based on the eigenvalues of the quantum-mechanical electronic stress tensor $\boldsymbol{\sigma}(\mathbf{r})$ at the saddle-type equilibrium points of $\nabla\rho(\mathbf{r})$ was previously proposed in reference [81].

Computational details

In the present work, *ab initio* computations were carried out for the following isolated, electrically neutral tight ion pairs and molecules: LiF, LiH, HF, BN, CO, NO, N_2, N_2H_4, N_2O_4, H_2O_2, and F_2. The geometries of these systems were optimized *in vacuo* using the Gaussian 16 program package [82] with the aug-cc-pVQZ basis sets [83–85]. In order to obtain correlated wave functions, the post-Hartree–Fock coupled-cluster method CCSD(full) [86–88] was used, with an unrestricted treatment for nitric oxide in its doublet state and a restricted treatment for the remaining systems in their singlet states; the following route-section keywords were specified: Density=Current, Pop=NO (or Pop=NOAB for the nitric oxide molecule), and Output=WFN. In each case, the natural orbital occupation numbers were verified to lie in the range from 0 to 2 and to sum to the correct number of electrons. For the optimized configurations, all vibrational frequencies were real.

Subsequently, property calculations were mainly carried out using the Multiwfn 3.8 program [89, 90]. The electrostatic potential $\varphi_{\mathrm{es}}(\mathbf{r})$ was computed with the same program following the procedure described in reference [91]. To calculate, within the natural orbital formalism, the spin-up- and spin-down-conditioned components of the exchange–correlation two-electron density $\Gamma_{xc}(\mathbf{r},\mathbf{r}')$, denoted by $\Gamma_{xc}^{\uparrow,\mathrm{total}}(\mathbf{r},\mathbf{r}')$ and $\Gamma_{xc}^{\downarrow,\mathrm{total}}(\mathbf{r},\mathbf{r}')$, the approximate Müller relation was used [92], as implemented in Multiwfn:

$$\Gamma_{xc}^{\uparrow,\mathrm{total}}(\mathbf{r},\mathbf{r}') \cong -\sum_{i\in\uparrow}\sum_{j\in\uparrow}\sqrt{\eta_i\eta_j}\phi_i^*(\mathbf{r})\,\phi_j^*(\mathbf{r}')\phi_j(\mathbf{r})\phi_i(\mathbf{r}'), \tag{41}$$

$$\Gamma_{xc}^{\downarrow,\mathrm{total}}(\mathbf{r},\mathbf{r}') \cong -\sum_{i\in\downarrow}\sum_{j\in\downarrow}\sqrt{\eta_i\eta_j}\phi_i^*(\mathbf{r})\,\phi_j^*(\mathbf{r}')\phi_j(\mathbf{r})\phi_i(\mathbf{r}'), \tag{42}$$

where ϕ_i and ϕ_j are natural spin orbitals, and η_i and η_j are their occupation numbers.

The electrostatic force field $\mathbf{F}_{\mathrm{es}}(\mathbf{r}) = -\nabla[-\varphi_{\mathrm{es}}(\mathbf{r})]$, the total static force field $\mathcal{F}(\mathbf{r}) = -\nabla\varphi_{\mathrm{em}}(\mathbf{r})$, and the exchange–correlation charge density $q_{xc}(\mathbf{r}) = -\nabla^2\varphi_{xc}^{\mathrm{hole}}(\mathbf{r})/(4\pi)$ were evaluated and analyzed using the in-house-developed VectorLab program, which implements a numerical differentiation scheme based on second-order-accurate central differences [14]. For this purpose, the required data grids were generated in Multiwfn with a step size of 0.02 a.u. The ContourLab program was employed for the preparation and analysis of contour maps. The electron delocalization indices $\delta\left(\Omega_S^{\mathrm{A}}, \Omega_S^{\mathrm{B}}\right)$ [53, 54] were determined using the AIMAll software package [93].

Additionally, to enable comparison, contour maps of the exchange-only charge density $q_x(\mathbf{r})$ for the boron nitride, hydrogen peroxide, and difluorine molecules were constructed. For this purpose, single-determinant wave functions corresponding to the newly optimized geometries of BN, H_2O_2, and F_2 were calculated at the Hartree–Fock [94, 95] and Kohn–Sham (RωB97X-D) [96] levels. Unless otherwise stated, the results presented and discussed were obtained from the single-reference multideterminant CCSD(full) wave functions.

Results and discussion

Figures 1 and 2 show superpositions of the calculated trajectory maps of the electron density gradient field $\nabla\rho(\mathbf{r})$, the per-electron electrostatic force field $\mathbf{F}_{\mathrm{es}}(\mathbf{r})$, and the Slater total static force field $\mathcal{F}(\mathbf{r})$ for the electrically neutral many-electron multinuclear systems under investigation. Figure 1 reveals a fairly simple pattern for the six polar diatomic ion pairs or molecules $\omega\alpha$ considered here. Importantly, this pattern was anticipated on the basis of our previous studies. First, the interatomic boundary $S(\alpha|\omega)$ lies closer to the nucleus ω of the electron-donor atom, whereas the interpseudoatomic boundary $U(\alpha|\omega)$ lies closer to the nucleus α of the electron-acceptor atom. Thus, in each of the six cases, an interbasin intersection of the $\Omega_S^{\alpha} \cap \Omega_U^{\omega}$ type occurs in the internuclear region, directly indicating the $\omega \rightarrow \alpha$ interatomic electronic charge transfer (see the "Theoretical background" section). The electronic charge contained in this intersection, $\iiint_{(\Omega_S^{\alpha} \cap \Omega_U^{\omega})} \rho(\mathbf{r})\mathrm{d}(\Omega_S^{\alpha} \cap \Omega_U^{\omega})$, contributes to the resulting electron populations of the atomic basins Ω_S^{ω} and Ω_S^{α} and fully

determines the positive charge of the electron-donor atom ω and the negative charge of the electron-acceptor atom α. The atomic charges $Q_{\nabla\rho}$ are reported in Table 1.

Second, each $\Omega_S^\alpha \cap \Omega_U^\omega$ interbasin intersection is accompanied by a nested $\Omega_S^\alpha \cap \Omega_P^\omega$ interbasin intersection that has a smaller volume and, consequently, a lower electron population (Fig. 1). The electronic charge contained in the latter intersection, $\iiint_{(\Omega_S^\alpha \cap \Omega_P^\omega)} \rho(\mathbf{r})\mathrm{d}(\Omega_S^\alpha \cap \Omega_P^\omega)$, determines the positive charge on the ω-centered cationic $\mathcal{F}$-pseudoatom and the negative charge on the α-centered anionic $\mathcal{F}$-pseudoatom. The force-field pseudoatomic charges $Q_\mathcal{F}$ for the analyzed $\omega\alpha$ systems are listed in Table 1. Table 1 shows that, in every case, the magnitude of atomic charging is greater than that of $\mathcal{F}$-pseudoatomic charging. It is also noteworthy that the magnitude of $\mathcal{F}$-pseudoatomic charging in the tight ion pairs LiF and LiH is appreciably greater than that in the remaining four polar molecules. Furthermore, a characteristic feature of the interatomic interactions in lithium fluoride and lithium hydride (Fig. 1a and b) is that the penetration depth of Ω_S^α into Ω_P^ω is markedly smaller than that into Ω_U^ω, indicating a weaker spatial manifestation of the electron-transfer-induced quantum chemical response (see the "Theoretical background" section). By contrast, for each of the polar covalent bonds shown in Fig. 1c–f, the zero-flux surface $P(\alpha|\omega)$ tends to approach the zero-flux surface $U(\alpha|\omega)$ at least in the vicinity of the internuclear line, indicating that the quantum chemical response is spatially more pronounced than in the two preceding cases. This behavior is reflected in the $Q_\mathcal{F}/Q_{\nabla\rho}$ ratios reported in Table 1; recall that $Q_\mathcal{F}/Q_{\nabla\rho}$ is interpreted as the fraction of the atomic charge attributable to its ionic (noncovalent) component. Smaller values of $Q_\mathcal{F}$ and $Q_\mathcal{F}/Q_{\nabla\rho}$ quantitatively indicate a more pronounced quantum chemical response. In this context, the relatively high $Q_\mathcal{F}$ and $Q_\mathcal{F}/Q_{\nabla\rho}$ values for the atoms in LiH indicate the coordinative character of the seemingly purely ionic Li···H interaction.

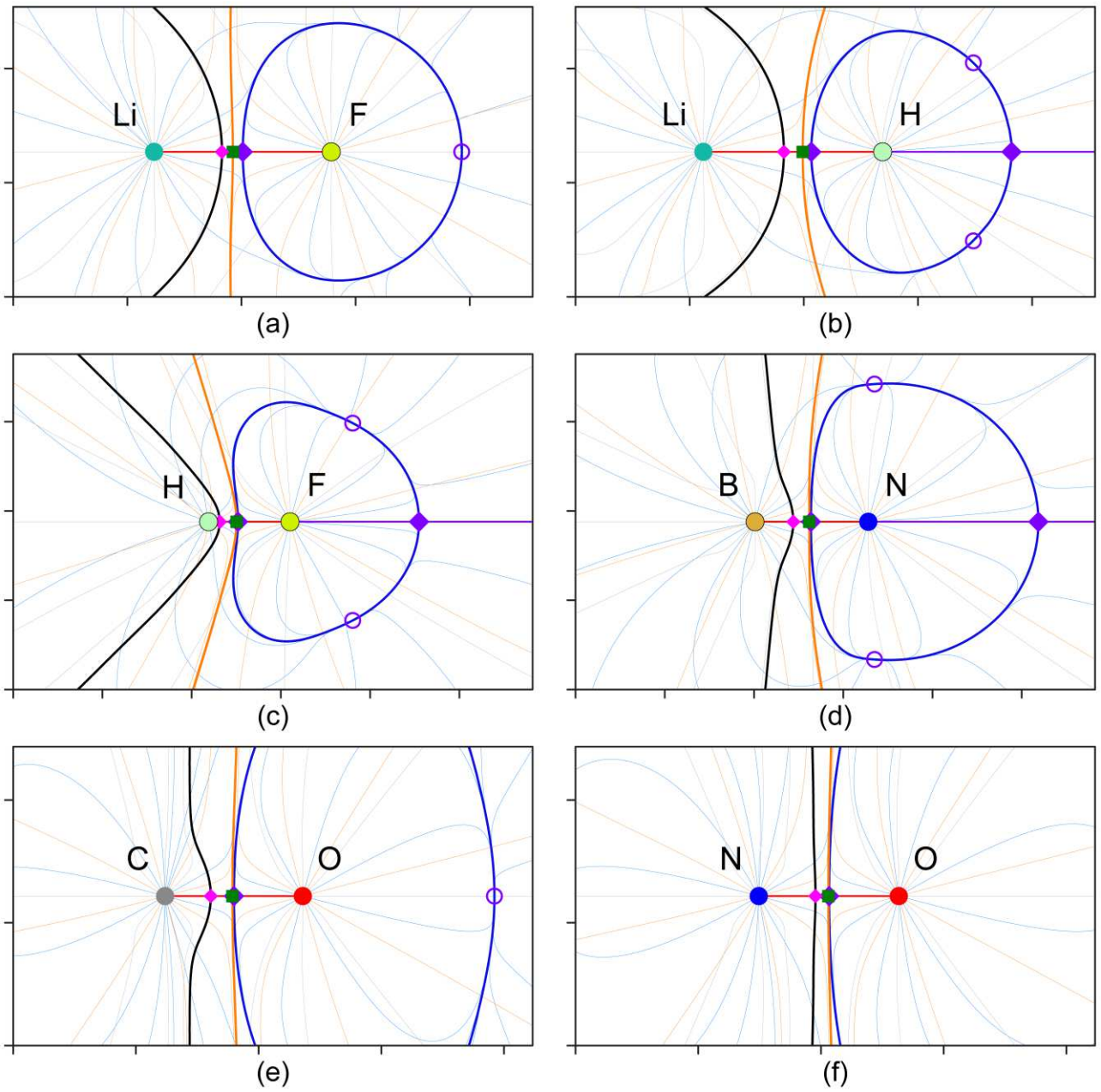

Fig. 1 Superpositions of the trajectory maps of the electron density gradient field $\nabla\rho(\mathbf{r})$ (black), the per-electron electrostatic force field $\mathbf{F}_{\mathrm{es}}(\mathbf{r})$ (blue), and the Slater total static force field $\mathcal{F}(\mathbf{r})$ (orange) for (**a**) lithium fluoride (LiF), (**b**) lithium hydride (LiH), (**c**) hydrogen fluoride (HF), (**d**) boron nitride (BN), (**e**) carbon monoxide (CO), and (**f**) nitric oxide (NO), all treated *in vacuo*. The traces of the zero-flux surfaces S, U, and P, determined in $\nabla\rho(\mathbf{r})$, $\mathbf{F}_{\mathrm{es}}(\mathbf{r})$, and $\mathcal{F}(\mathbf{r})$, respectively, are indicated by thick lines of the corresponding colors. The nuclear positions are denoted by solid circles. The line-type saddle equilibrium points in $\nabla\rho(\mathbf{r})$, $\mathbf{F}_{\mathrm{es}}(\mathbf{r})$, and $\mathcal{F}(\mathbf{r})$ are shown as filled magenta rhombuses, filled violet rhombuses, and filled green squares, respectively. The source equilibrium points in $\mathbf{F}_{\mathrm{es}}(\mathbf{r})$ are denoted by hollow violet circles. The trajectory paths in $\nabla\rho(\mathbf{r})$, $\mathbf{F}_{\mathrm{es}}(\mathbf{r})$, and $\mathcal{F}(\mathbf{r})$ are depicted as red, violet, and green lines, respectively. The distance between adjacent tick marks on the axes is 1 Å

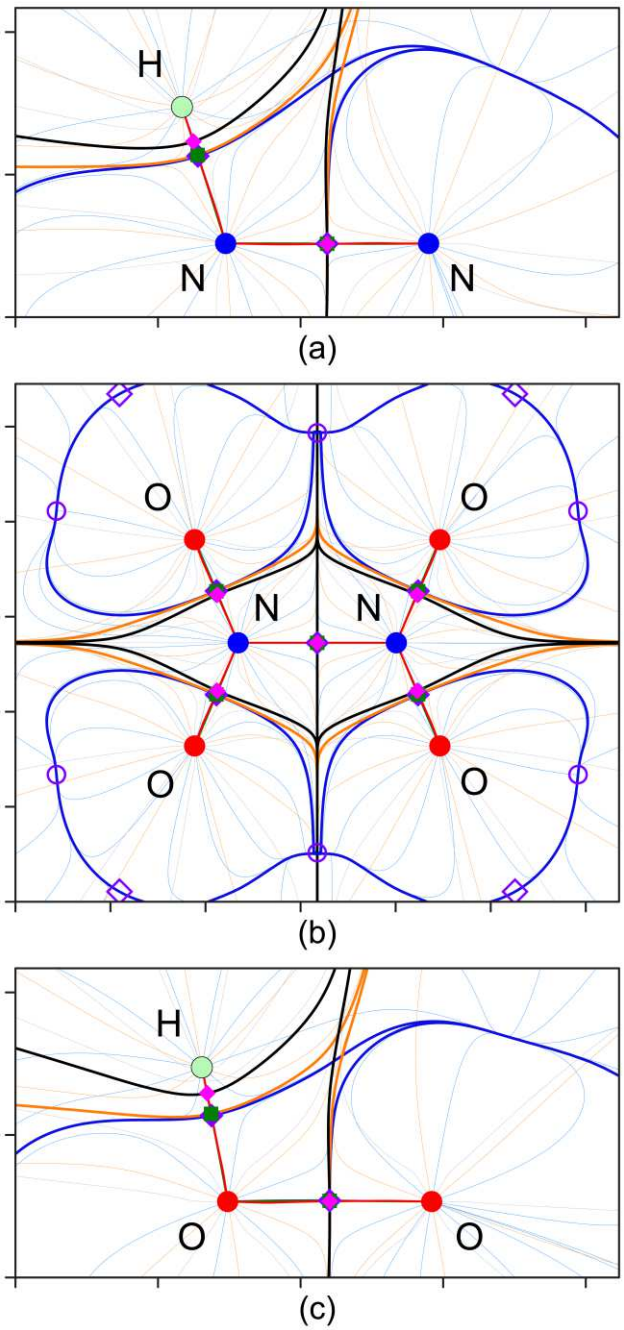

Fig. 2 Superpositions of the trajectory maps of the electron density gradient field $\nabla\rho(\mathbf{r})$ (black), the per-electron electrostatic force field $\mathbf{F}_{\mathrm{es}}(\mathbf{r})$ (blue), and the Slater total static force field $\mathcal{F}(\mathbf{r})$ (orange) for (**a**) hydrazine (N_2H_4), (**b**) dinitrogen tetroxide (N_2O_4), and (**c**) hydrogen peroxide (H_2O_2), all treated *in vacuo*. The traces of the zero-flux surfaces S, U, and P, determined in $\nabla\rho(\mathbf{r})$, $\mathbf{F}_{\mathrm{es}}(\mathbf{r})$, and $\mathcal{F}(\mathbf{r})$, respectively, are indicated by thick lines of the corresponding colors. The nuclear positions are denoted by solid circles. The line-type saddle equilibrium points in $\nabla\rho(\mathbf{r})$, $\mathbf{F}_{\mathrm{es}}(\mathbf{r})$, and $\mathcal{F}(\mathbf{r})$ are shown as filled magenta rhombuses, filled violet rhombuses, and filled green squares, respectively. The cycle-type saddle and source equilibrium points in $\mathbf{F}_{\mathrm{es}}(\mathbf{r})$ are denoted by hollow violet rhombuses and hollow violet circles, respectively. The internuclear paths in $\nabla\rho(\mathbf{r})$, $\mathbf{F}_{\mathrm{es}}(\mathbf{r})$, and $\mathcal{F}(\mathbf{r})$ are depicted as red, violet, and green lines, respectively. The distance between adjacent tick marks on the axes is 1 Å

Table 1 Numerically integrated charges of the anionic atoms and the corresponding anionic force-field pseudoatoms, together with the ratios of these charges, in the systems studied [a]

System $\omega\alpha$ [b]	$Q_{\nabla\rho}$, e	$Q_{\mathcal{F}}$, e	$Q_{\mathcal{F}}/Q_{\nabla\rho}$
LiF	–0.932	–0.652	0.70
LiH	–0.905	–0.403	0.45
HF	–0.760	–0.273	0.36
BN	–1.313	–0.260	0.20
CO	–1.256	–0.152	0.12
NO	–0.461	–0.056	0.12

[a] The calculated pseudoatomic charges $Q_{\mathbf{F}_{\mathrm{es}}}$ are consistent with the expected value of 0.00 e. [b] In the notation adopted in the present work, a polar diatomic ion pair or molecule is written as $\omega\alpha$, with the electron-donor center ω listed first and the electron-acceptor center α listed second

Analysis of the interbasin intersections in the trajectory maps shown in Fig. 2 indicates that, in each of the following interatomic interactions—the H–N bonds in hydrazine, the N–O bonds in dinitrogen tetroxide, and the H–O bonds in hydrogen peroxide—the atom listed first is the electron donor (ω), whereas the atom listed second is the electron acceptor (α). Indeed, the physical charges $Q_{\nabla\rho}$ of the atoms listed second are –0.742 e, –0.407 e, and –0.603 e, respectively. On the basis of the degree to which the quantum chemical response is manifested spatially, these interatomic interactions may be classified as polar covalent. The corresponding pseudoatomic charges $Q_{\mathcal{F}}$ are –0.223 e, –0.156 e, and –0.211 e, respectively. The trajectory maps in Fig. 2 reveal no distinctive features for the nonpolar axial bonds, including any attributable to the charge-shift (or electron-pair-deficient) character of the homoatomic bonds in N_2O_4 and H_2O_2. In particular, for every bond in Figs. 1 and 2, there is one corresponding internuclear path in each of the vector fields $\nabla\rho(\mathbf{r})$, $\mathbf{F}_{\mathrm{es}}(\mathbf{r})$, and $\mathcal{F}(\mathbf{r})$. Notably, in these cases, bonding and binding occur between atoms with substantial like-signed atomic charges, and the corresponding force-field pseudoatoms carry like-signed charges of smaller but still appreciable magnitude. Overall, it has been demonstrated that, when Coulomb correlation is explicitly accounted for—that is, when the theoretical analysis is based on correlated wave functions—the manifestation of electron-transfer-induced quantum chemical response retains its expected pattern.

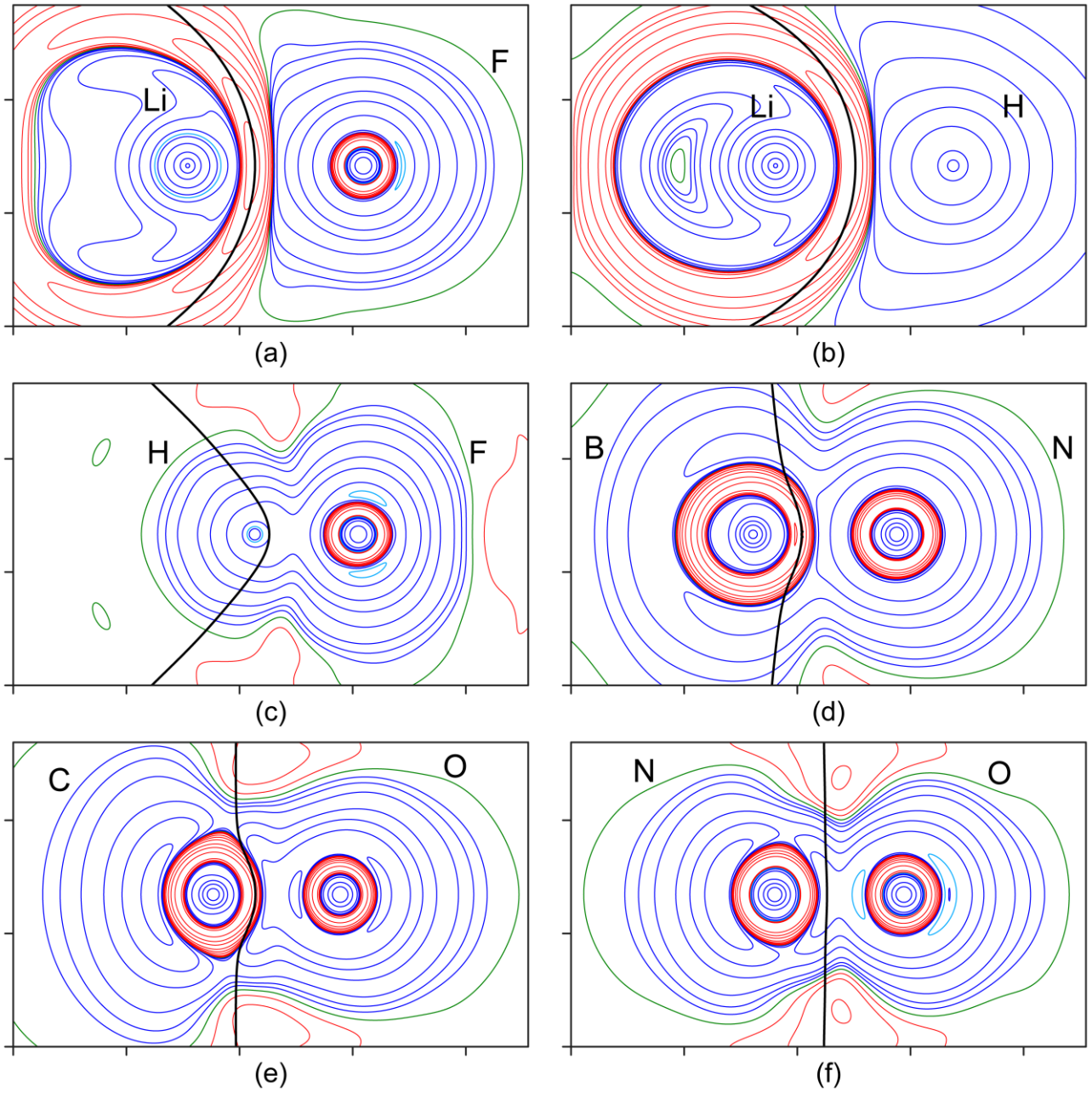

Fig. 3 Contour maps of the Slater exchange–correlation charge density $q_{xc}(\mathbf{r})$ for (**a**) lithium fluoride (LiF), (**b**) lithium hydride (LiH), (**c**) hydrogen fluoride (HF), (**d**) boron nitride (BN), (**e**) carbon monoxide (CO), and (**f**) nitric oxide (NO), all treated *in vacuo*. Blue, green, and red isocontours correspond to negative, zero, and positive values of $q_{xc}(\mathbf{r})$, respectively. Contours are drawn at 0, $\pm 2 \cdot 10^n$, $\pm 4 \cdot 10^n$, and $\pm 8 \cdot 10^n$ a.u. ($-3 \leq n \leq 0$; $n \in \mathbb{Z}$), with an extra isocontour at –20 a.u. added to all panels except (**b**); because the corresponding levels lie outside the respective data ranges, the contours at 4 and 8 a.u. are absent from panels (**a**), (**c**), (**e**), and (**f**), those at or above 0.2 a.u. are absent from (**b**), and those at 2, 4, and 8 a.u. are absent from (**d**). Contours at additional levels of –0.3 a.u. in panels (**a**) and (**c**) and –0.17 a.u. in panel (**f**) are included and highlighted in light blue. The traces of the zero-flux surfaces S, determined in the electron density gradient field $\nabla\rho(\mathbf{r})$, are shown as solid black lines. The distance between adjacent tick marks on the axes is 1 Å

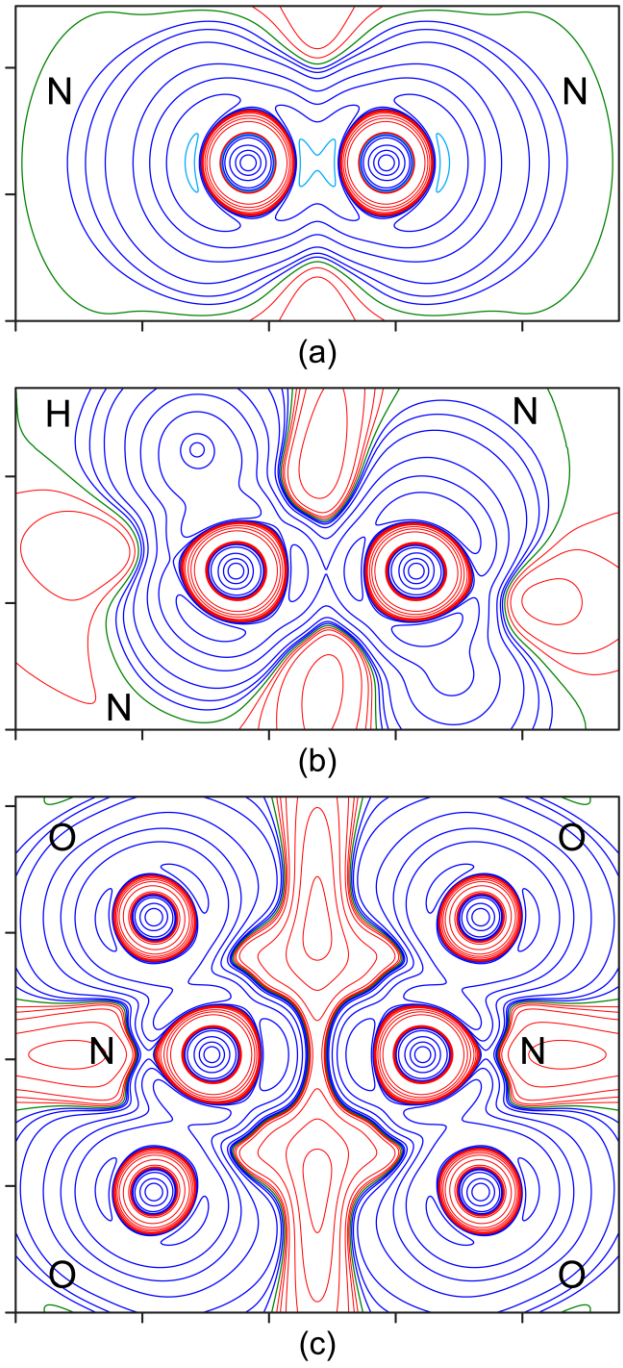

Fig. 4 Contour maps of the Slater exchange–correlation charge density $q_{xc}(\mathbf{r})$ for (**a**) dinitrogen (N_2), (**b**) hydrazine (N_2H_4), and (**c**) dinitrogen tetroxide (N_2O_4), all treated *in vacuo*. Blue, green, and red isocontours correspond to negative, zero, and positive values of $q_{xc}(\mathbf{r})$, respectively. Contours are drawn at 0, $\pm 2 \cdot 10^n$, $\pm 4 \cdot 10^n$, and $\pm 8 \cdot 10^n$ a.u. ($-3 \leq n \leq 0$; $n \in \mathbb{Z}$), with an extra isocontour at –20 a.u.; because the corresponding levels lie outside the respective data ranges, the contours at 2, 4, and 8 a.u. are absent from panels (**a**) and (**b**), whereas the contours at 4 and 8 a.u. are absent from panel (**c**). Contours at an additional level of –0.15 a.u. in panel (**a**) are included and highlighted in light blue. The distance between adjacent tick marks on the axes is 1 Å

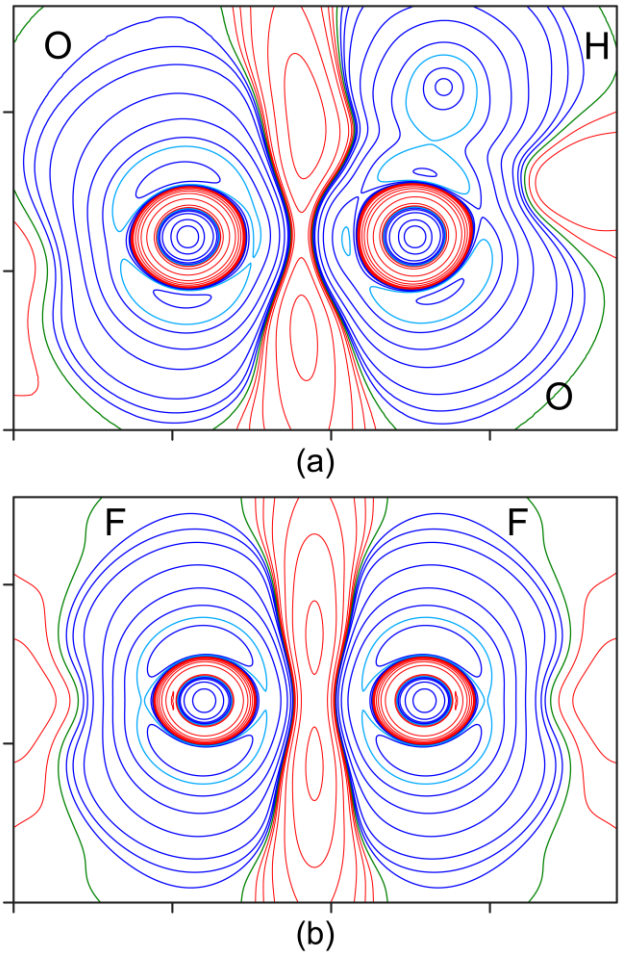

Fig. 5 Contour maps of the Slater exchange–correlation charge density $q_{xc}(\mathbf{r})$ for (**a**) hydrogen peroxide (H_2O_2) and (**b**) difluorine (F_2), both treated *in vacuo*. Blue, green, and red isocontours correspond to negative, zero, and positive values of $q_{xc}(\mathbf{r})$, respectively. Contours are drawn at 0, $\pm 2 \cdot 10^n$, $\pm 4 \cdot 10^n$, and $\pm 8 \cdot 10^n$ a.u. ($-3 \leq n \leq 0$; $n \in \mathbb{Z}$), with an extra isocontour at –20 a.u.; the contours at 4 and 8 a.u. in panel (**a**) and at 8 a.u. in panel (**b**) are absent because these values lie outside the respective data ranges. Contours at additional levels of –0.115 a.u. in panel (**a**) and –0.14 a.u. in panel (**b**) are included and highlighted in light blue. The distance between adjacent tick marks on the axes is 1 Å

Figures 3, 4, and 5 present contour maps of the Slater exchange–correlation charge density $q_{xc}(\mathbf{r})$ for the systems under investigation. Negative values of $q_{xc}(\mathbf{r})$ allow regions of electron-pair density condensation to be identified (see the "Theoretical background" section). In these maps, such regions are observed in atomic core shells, in areas associated with lone electron pairs, and between the cores of some bonded atoms. By contrast, positive values of $q_{xc}(\mathbf{r})$ indicate electron-pair density decondensation. Several important features evident from Fig. 3 merit particular attention. First, Fig. 3 illustrates the compression of the *K* shells of second-period atoms with increasing atomic number.

The maps further indicate that $q_{xc}(\mathbf{r})$ may provide valuable information on the internal structure of atomic cores; a detailed analysis of this aspect of atomic structure lies beyond the scope of the present work and should be pursued in future studies. Second, the localization of lone electron pairs is reflected in the distribution of $q_{xc}(\mathbf{r})$ by deep wells in the antibonding regions. The CO and NO molecules provide illustrative examples: these wells with $q_{xc}(\mathbf{r}) < 0$ are observed on both extensions of the bond axis in each molecule (Fig. 3e and f). Third, inspection of the $q_{xc}(\mathbf{r})$ distributions reveals that the spatial separation between regions of electron-pair density decondensation and condensation is pronounced for the tight ion pairs LiF and LiH (Fig. 3a and b), whereas typical polar covalent bonds exhibit electron-pair density condensation in their internuclear binding regions (Fig. 3c–f). It is also worth noting that a comparison of the distributions of the exchange-only charge density $q_x(\mathbf{r})$ (Figs. 6 and 7) and the exchange–correlation charge density $q_{xc}(\mathbf{r})$ (Figs. 3d and 5) suggests that the effects of Coulomb correlation can appreciably shape the real-space pattern of electron-pair density (de)condensation.

Providing an electron pair (or an analog thereof) for a Lewis acid–base interaction does not establish the direction of interatomic electron transfer. In noncovalent or metal-coordination interactions, the base supplies the electron pair to the internuclear binding region (usually without physically donating it to the acid), orienting it toward an electron-pair-deficient region of the acid's valence shell [5, 24, 26]. Treating the Lewis base as necessarily an electron-density donor (a contributor in our earlier terminology) and the Lewis acid as necessarily an electron-density acceptor (an occupier) is a persistent error (as reflected, for example, in the review [97]): interatomic electronic charge transfer often—but not always [18]—proceeds from the acid to the base. LiF and LiH illustrate this point. Their $q_{xc}(\mathbf{r})$ distributions identify Li as the Lewis acid and F and H as the respective bases (Fig. 3a and b), whereas their atomic charges (Table 1) and the relative positions of the zero-flux boundaries S and U (Fig. 1a and b) establish that Li is the electron-density donor and F and H are the acceptors. The conventional donor–acceptor assignment is thus contradicted even by these simple ion pairs.

The following presentation and discussion of the results focus on electron-pair-deficient homoatomic covalent bonds, on the real-space manifestations of the charge-shift bonding mechanism in such bonds, and on their nature from a force-field and charge-density perspective. Table 2 reports values of the delocalization index $\delta\left(\Omega_S^{\mathrm{A}}, \Omega_S^{\mathrm{B}}\right)$ and the internuclear potential-barrier height $\varphi_{\mathrm{em}}(\mathbf{r}_\pi)$ (see the "Theoretical background" section). Although $\delta\left(\Omega_S^{\mathrm{A}}, \Omega_S^{\mathrm{B}}\right)$ decreases appreciably and $\varphi_{\mathrm{em}}(\mathbf{r}_\pi)$ increases markedly along the series from the electron-pair-rich N–N bond in N_2 through the N–N bond in N_2H_4 to the electron-pair-deficient N–N bond in N_2O_4, the O–O bond in H_2O_2 and the F–F bond in F_2, both regarded as standard examples of charge-shift bonding, exhibit relatively high values of $\delta\left(\Omega_S^{\mathrm{A}}, \Omega_S^{\mathrm{B}}\right)$ and relatively low values of $\varphi_{\mathrm{em}}(\mathbf{r}_\pi)$. For example, the value of $\varphi_{\mathrm{em}}(\mathbf{r}_\pi)$ for the F–F bond—a prototypical charge-shift bond—is even lower than that for the N–N bond in N_2H_4 (Table 2). Thus, it may be concluded that $\delta\left(\Omega_S^{\mathrm{A}}, \Omega_S^{\mathrm{B}}\right)$ and $\varphi_{\mathrm{em}}(\mathbf{r}_\pi)$ do not provide a clear indication of the electron-pair-deficient (or charge-shift) character of nonpolar covalent bonds.

Table 2 Selected properties of interatomic interactions in the systems studied

System	Internuclear distance, Å	$\delta\left(\Omega_S^{\mathrm{A}}, \Omega_S^{\mathrm{B}}\right)$	$\varphi_{\mathrm{em}}(\mathbf{r}_\pi)$, a.u.	$\Lambda_1(\mathbf{r}_\pi)$, a.u.	$\Lambda_2(\mathbf{r}_\pi)$, a.u.	$\Lambda_3(\mathbf{r}_\pi)$, a.u.	$\Xi(\mathbf{r}_\pi)$	$q_{xc}(\mathbf{r}_\pi)$, a.u.
LiF	1.55212	0.191	–1.268	–4.238	1.000	1.000	4.240	0.079
LiH	1.57022	0.201	–0.880	–1.769	0.563	0.563	3.145	–0.002
HF	0.91395	0.392	–2.678	–18.256	6.803	6.803	2.683	–0.107
BN	1.26906	1.678	–2.472	–9.609	3.384	3.384	2.839	–0.054
CO	1.12216	1.407	–3.1875	–17.182	5.397	5.397	3.184	–0.126
NO	1.14099	1.864	–3.1876	–17.817	5.418	5.617	3.229	–0.109
N_2	1.09094	2.330	–3.392	–19.482	6.165	6.165	3.160	–0.153
$H_2N–NH_2$ [a]	1.42338	1.028	–2.007	–8.079	2.291	2.296	3.523	–0.040
$O_2N–NO_2$ [a]	1.66453	0.498	–1.646	–4.992	1.163	1.164	4.291	0.011
HO–OH [a]	1.43088	0.997	–1.993	–8.753	2.364	2.429	3.652	0.015
F_2	1.38739	0.915	–2.129	–10.461	2.840	2.840	3.684	0.074

[a] The data are presented for the axial homoatomic bonds

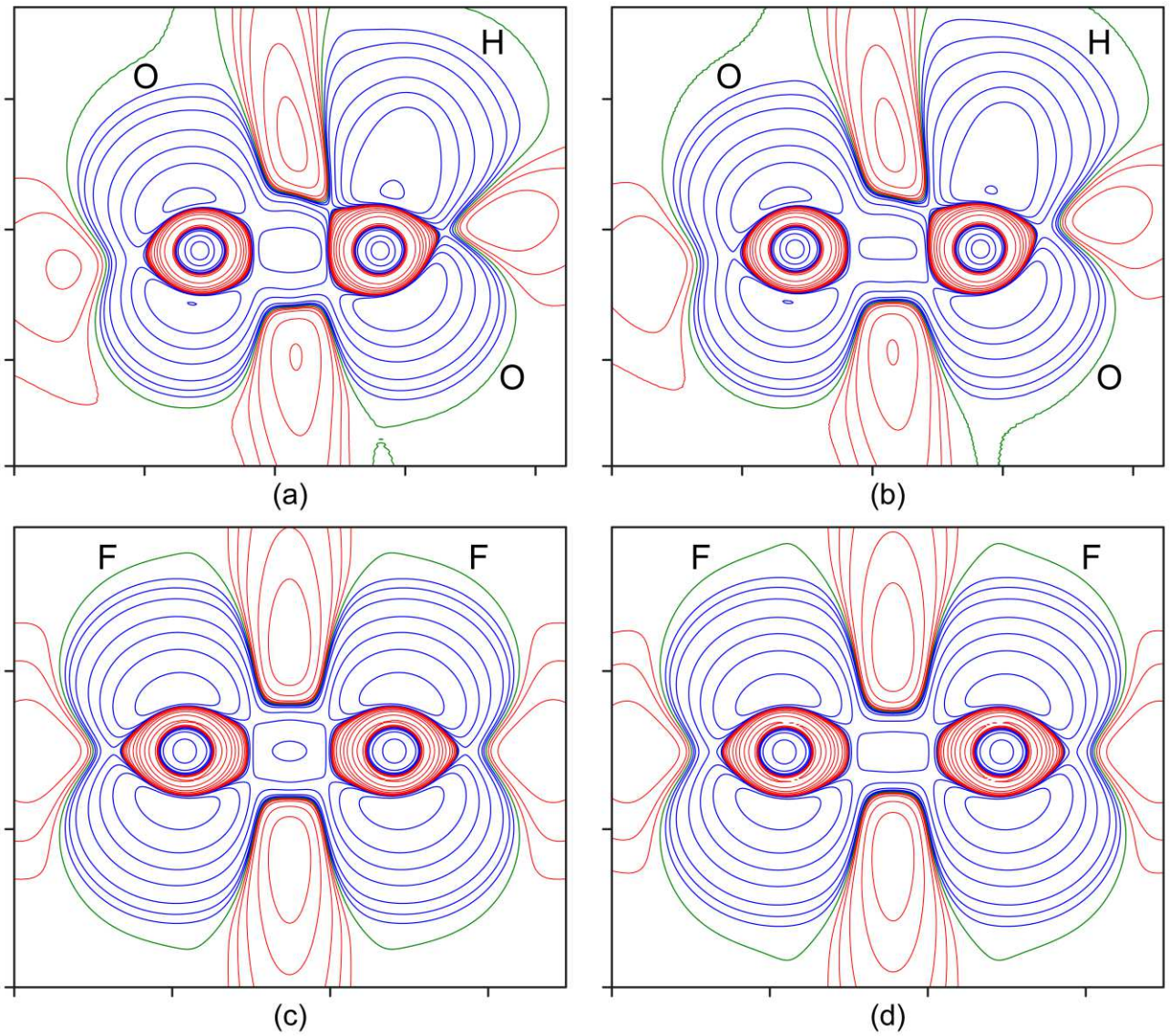

Fig. 6 Contour maps of the Slater exchange-only charge density $q_x(\mathbf{r})$ for (**a** and **b**) hydrogen peroxide (H_2O_2) and (**c** and **d**) difluorine (F_2), both treated *in vacuo*. Panels (**a**) and (**c**) show results obtained at the Hartree–Fock level, whereas panels (**b**) and (**d**) show those obtained at the Kohn–Sham (RωB97X-D) level. Blue, green, and red isocontours correspond to negative, zero, and positive values of $q_x(\mathbf{r})$, respectively. Contours are drawn at 0, $\pm 2\cdot 10^n$, $\pm 4\cdot 10^n$, and $\pm 8\cdot 10^n$ a.u. ($-3 \leq n \leq 0$; $n \in \mathbb{Z}$), with an extra isocontour at –20 a.u.; because the corresponding levels lie outside the respective data ranges, the contours at 4 and 8 a.u. are absent from panels (**a**) and (**b**), whereas the contours at 8 a.u. are absent from panels (**c**) and (**d**). The distance between adjacent tick marks on the axes is 1 Å

The discussion now turns to the quantity $\Xi(\mathbf{r}_\pi)$, defined as the ratio of the absolute value of the tensile-mode eigenvalue, $|\Lambda_1(\mathbf{r}_\pi)|$, to the average of the two compressive-mode eigenvalues $\Lambda_2(\mathbf{r}_\pi)$ and $\Lambda_3(\mathbf{r}_\pi)$ [see Eq. (40) and the "Theoretical framework" section]. Table 2 indicates that $\Xi(\mathbf{r}_\pi)$ increases systematically along the aforementioned series of N–N covalent bonds from its electron-

pair-rich to its electron-pair-deficient member. Moreover, the values of $\Xi(\mathbf{r}_\pi)$ for the O–O bond in H_2O_2 and the F–F bond in F_2 are slightly but noticeably higher than the corresponding value for the N–N bond in N_2H_4. Thus, relative to the compressive principal modes, the tensile principal mode of the local linear variation of the scalar Cartesian components of $\mathcal{F}(\mathbf{r})$ is more pronounced in charge-shift bonds than in conventional covalent bonds (*e.g.*, the N–N bond in N_2), with *the tensile mode representing attraction of the electron cloud toward the nuclei* and the *compressive modes representing attraction of the electron cloud toward the bond axis*. A similar conclusion regarding the real-space mechanism of charge-shift bonding was reached in the study reported in reference [81], in which the eigenvalues of the electronic stress tensor $\boldsymbol{\sigma}(\mathbf{r})$ were analyzed instead.

As is evident from Figs. 4 and 5, charge-shift bonding is manifested in real space in the $q_{xc}(\mathbf{r})$ representation as *electron-pair density decondensation*—with Coulomb correlation explicitly accounted for as a contributing factor—within internuclear binding regions. Indeed, the well-established homoatomic charge-shift bonds—namely, the N–N bond in N_2O_4 (Fig. 4c), the O–O bond in H_2O_2 (Fig. 5a), and the F–F bond in F_2 (Fig. 5b)—exhibit *positive* values of $q_{xc}(\mathbf{r})$ at the midpoint between the nuclei. On this basis, covalent bonds whose internuclear binding regions exhibit such decondensation, as indicated by positive values of $q_{xc}(\mathbf{r})$, are proposed to constitute a distinct class, here termed *electron-pair-deficient covalent bonds*. According to Table 2, the values of $q_{xc}(\mathbf{r}_\pi)$ for these three interatomic interactions exceed 0.01 a.u., with the highest value occurring for F–F. A recent study [98] reported positive values of the divergence of the exchange–correlation Ehrenfest force density field, $\nabla \cdot \mathbf{F}_{xc}^{\mathrm{Ehr}}(\mathbf{r}) = \nabla \cdot [\mathfrak{F}(\mathbf{r}) - \rho(\mathbf{r})\mathbf{F}_{\mathrm{es}}(\mathbf{r})]$, between the fluorine atomic cores in F_2; the function $\nabla \cdot \mathbf{F}_{xc}^{\mathrm{Ehr}}(\mathbf{r})$ is formally similar to $q_{xc}(\mathbf{r})$ and $q_{xc}^{\mathrm{Ehr}}(\mathbf{r}) = \nabla \cdot [\{\mathfrak{F}(\mathbf{r})/\rho(\mathbf{r})\} - \mathbf{F}_{\mathrm{es}}(\mathbf{r})]/(4\pi)$ but is not proportional to charge density [27]. It is also noteworthy that, at both the Hartree–Fock and Kohn–Sham levels, the Slater exchange-only charge density $q_x(\mathbf{r})$ takes negative values at the midpoints of the O–O bond in H_2O_2 and the F–F bond in F_2 (Fig. 6). Finally, in addition to the $q_{xc}(\mathbf{r}_\pi)$ values, the character of the $q_{xc}(\mathbf{r})$ distribution in the internuclear region warrants particular consideration. For instance, two pronounced wells of negative charge

density occur along the N–N bond in N_2O_4 (Fig. 4c). This pattern indicates that electron-pair density supplied by the two N atoms remains localized in the internuclear binding region, although it is split into two distinct accumulations. Similar wells are less pronounced along the O–O bond in H_2O_2 (Fig. 5a) and are not characteristic of the F–F bond in F_2 (Fig. 5b). Furthermore, the N–N bond in N_2H_4, in which the charge-shift bonding mechanism is considered to operate in a tempered manner [31], has a negative $q_{xc}(\mathbf{r}_\pi)$ value of –0.040 a.u. (Table 2), but its $q_{xc}(\mathbf{r})$ distribution is characterized by two distinct wells (Fig. 4b).

Conclusions

The present study yields the following principal findings. First, it has been demonstrated that, when Coulomb correlation is explicitly accounted for, the manifestation of electron-transfer-induced quantum chemical response retains its expected qualitative pattern. This finding does not, however, rule out a reorganization of the nonclassical force field $\mathcal{F}(\mathbf{r}) - \mathbf{F}_{\mathrm{es}}(\mathbf{r})$ upon inclusion of Coulomb correlation, particularly with respect to the occurrence and properties of force-field basins with nonnuclear attractors [14, 16, 17, 23, 27]; this question warrants detailed investigation beyond the scope of the present work. Second, relative to the compressive principal modes, the tensile principal mode of the local linear variation of the scalar Cartesian components of the Slater total static force field $\mathcal{F}(\mathbf{r})$ is more pronounced in charge-shift bonds than in conventional homoatomic covalent bonds, with the tensile mode [eigenvalue $\Lambda_1(\mathbf{r}_\pi)$] representing attraction of the electron cloud toward the nuclei and the compressive modes [eigenvalues $\Lambda_2(\mathbf{r}_\pi)$ and $\Lambda_3(\mathbf{r}_\pi)$] representing attraction of the electron cloud toward the bond axis. Third, in the representation based on the Slater exchange–correlation charge density $q_{xc}(\mathbf{r}) = \nabla \cdot \mathbf{F}_{xc}(\mathbf{r})/(4\pi)$, charge-shift bonding is manifested in real space as electron-pair density decondensation within internuclear binding regions. In light of this finding, covalent bonds whose internuclear binding regions exhibit such decondensation, as indicated by positive values of $q_{xc}(\mathbf{r})$, are proposed to constitute a distinct class, here termed electron-pair-deficient covalent bonds. Finally, the effects of Coulomb correlation can appreciably shape electron-pair density condensation in real space, and from the force-field and charge-density perspective, this

influence may play a decisive role in the charge-shift bonding mechanism. In particular, the electron-pair-deficient character of charge-shift bonds appears to arise because electron-pair density condensation resulting from the Fermi–Pauli-correlation-induced attenuation of effective interelectronic repulsion is outweighed by decondensation resulting from Coulomb-correlation-induced enhancement of this repulsion, whereas in conventional covalent bonds the former effect substantially dominates the latter.

In addition, the Slater total static potential $\varphi_{\mathrm{em}}(\mathbf{r})$ acting on an electron in a many-electron chemical system is formally defined as the ratio of the expectation value of the local Coulomb interaction energy density operator to that of the local electron number density operator. In other words, $\varphi_{\mathrm{em}}(\mathbf{r})$ represents the mean Coulomb interaction energy of that electron with all the other charged particles of the electron–nuclear system—its atomic nuclei and remaining electrons. Grounded directly in the formalism of quantum mechanics, this definition provides a rigorous basis for deriving the following quantities: the eigenvalues $\Lambda_1(\mathbf{r})$, $\Lambda_2(\mathbf{r})$, and $\Lambda_3(\mathbf{r})$ of the Hessian of $\varphi_{\mathrm{em}}(\mathbf{r})$; the local source $\mathrm{LS}_{\varphi_{\mathrm{em}}}(\mathbf{r},\mathbf{r}')$ and the corresponding source function $\mathrm{SF}_{\varphi_{\mathrm{em}}}(\mathbf{r},\Omega_S)$, both defined for $\varphi_{\mathrm{em}}(\mathbf{r})$; the conservative force field $\mathcal{F}(\mathbf{r}) = -\nabla\varphi_{\mathrm{em}}(\mathbf{r})$; the effective charge density $q_{\mathrm{em}}(\mathbf{r}) = \nabla\cdot\mathcal{F}(\mathbf{r})/(4\pi) = -\sum_n Z_n\delta(\mathbf{r}-\mathbf{R}_n) + \rho(\mathbf{r}) + q_{xc}(\mathbf{r})$; the total effective atomic charge $Q_{\nabla\rho}^{\mathrm{eff}/\mathcal{F}} = -\iiint_{\Omega_S} q_{\mathrm{em}}(\mathbf{r})\mathrm{d}\Omega_S$; and the atomic Slater force $\mathcal{F}(\Omega_S) = \iiint_{\Omega_S}\mathcal{F}(\mathbf{r})\rho(\mathbf{r})\mathrm{d}\Omega_S$. The same definition justifies using these physical quantities, together with the potential itself, to elucidate chemical structure in real space, describe known physical phenomena and refine their interpretation, and identify and investigate new ones. This description of chemical structure is consistent with the principle of observability, including its interpretation for chemistry set out in references [26, 28].

Appendix

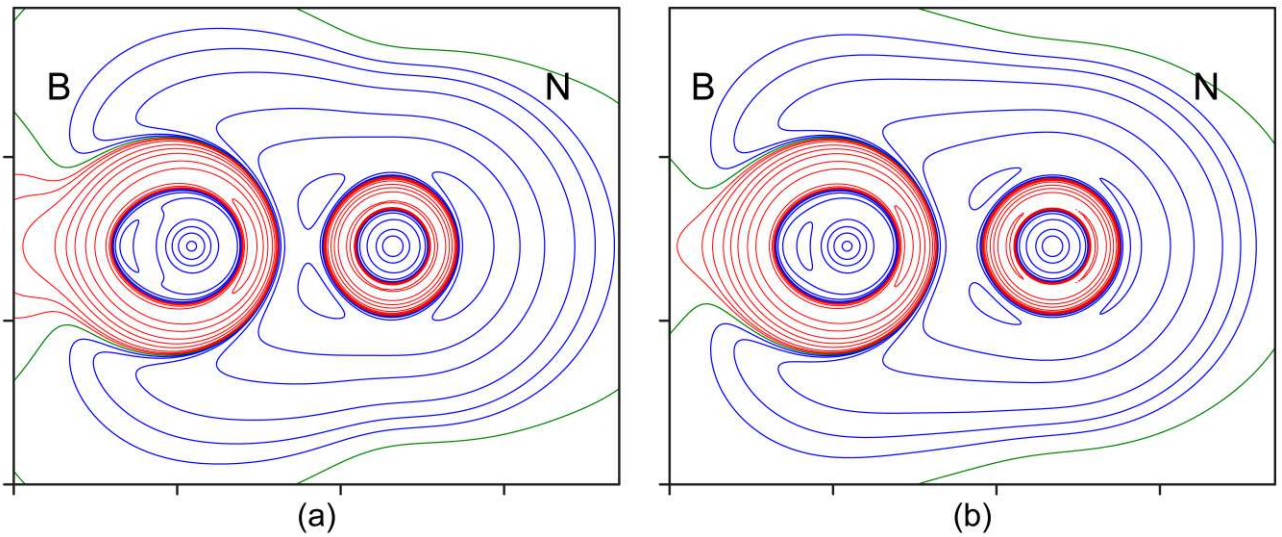

Fig. 7 Contour maps of the Slater exchange-only charge density $q_x(\mathbf{r})$ for boron nitride (BN), treated *in vacuo* at (**a**) the Hartree–Fock and (**b**) the Kohn–Sham (RωB97X-D) levels. Blue, green, and red isocontours correspond to negative, zero, and positive values of $q_x(\mathbf{r})$, respectively. Contours are drawn at 0, $\pm 2\cdot 10^n$, $\pm 4\cdot 10^n$, and $\pm 8\cdot 10^n$ a.u. ($-3 \le n \le 0$; $n \in \mathbb{Z}$), with an extra isocontour at –20 a.u.; the contours at 4 and 8 a.u. are absent because the corresponding levels lie outside the respective data ranges. The distance between adjacent tick marks on the axes is 1 Å

Author contributions

Sergey V. Kartashov: formal analysis; investigation; software; validation; visualization; writing – review & editing. Robert R. Fayzullin: conceptualization; data curation; formal analysis; funding acquisition; investigation; methodology; project administration; resources; supervision; validation; visualization; writing – original draft preparation; writing – review & editing.

Funding

This work was supported by a grant awarded by the Academy of Sciences of the Republic of Tatarstan to higher education institutions, research organizations, and other entities for the implementation of human resource development plans.

Data availability

No datasets were generated or analyzed during the current study. The in-house-developed VectorLab and ContourLab programs are available from the authors upon reasonable request.

Declarations

Ethics approval Not applicable.

Competing interests Sergey V. Kartashov declares no competing interests. Robert R. Fayzullin declares that he is a member of the Editorial Board of Structural Chemistry.

References

1. Shteingolts SA, Stash AI, Tsirelson VG, Fayzullin RR (2021) Orbital-free quantum crystallographic view on noncovalent bonding: insights into hydrogen bonds, π···π and reverse electron lone pair···π interactions. Chem Eur J 27:7789–7809. https://doi.org/10.1002/chem.202005497
2. Shteingolts SA, Voronina JK, Saifina LF, Shulaeva MM, Semenov VE, Fayzullin RR (2021) On the transfer of theoretical multipole parameters for restoring static electron density and revealing and treating atomic anharmonic motion. Features of chemical bonding in crystals of an isocyanuric acid derivative. Acta Crystallogr, Sect B: Struct Sci Cryst Eng Mater 77:871–891. https://doi.org/10.1107/S2052520621009690
3. Shteingolts SA, Stash AI, Tsirelson VG, Fayzullin RR (2022) Real-space interpretation of interatomic charge transfer and electron exchange effects by combining static and kinetic potentials and associated vector fields. Chem Eur J 28:e202200985. https://doi.org/10.1002/chem.202200985
4. Kartashov SV, Shteingolts SA, Stash AI, Tsirelson VG, Fayzullin RR (2023) Electronic and crystal packing effects in terms of static and kinetic force field features: picolinic acid N-oxide and methimazole. Cryst Growth Des 23:1726–1742. https://doi.org/10.1021/acs.cgd.2c01286
5. Saifina AF, Kartashov SV, Stash AI, Tsirelson VG, Fayzullin RR (2023) Unified picture of interatomic interactions, structures, and chemical reactions by means of electrostatic and kinetic force density fields: Appel's salt and its ion pairs. Cryst Growth Des 23:3002–3018. https://doi.org/10.1021/acs.cgd.3c00088
6. Takebayashi S, Ariai J, Gellrich U, Kartashov SV, Fayzullin RR, Kang H-B, Yamane T, Sugisaki K, Sato K (2023) Synthesis and characterization of a formal 21-electron cobaltocene derivative. Nat Commun 14:4979 https://doi.org/10.1038/s41467-023-40557-7
7. Saifina AF, Kartashov SV, Saifina LF, Fayzullin RR (2023) Applicability of transferable multipole pseudo-atoms for restoring inner-crystal electronic force density fields. Chemical bonding and binding features in the crystal and dimer of 1,3-bis(2-hydroxyethyl)-6-methyluracil. IUCrJ 10:584–602. https://doi.org/10.1107/S2052252523007108

8. Fayzullin RR (2023) Interatomic interactions in molecules, associates, crystals and transition states in terms of electronic force density fields. Acta Crystallogr, Sect A: Found Adv 79(a2):C498. https://doi.org/10.1107/S2053273323091179
9. Khrizanforova VV, Fayzullin RR, Kartashov SV, Morozov VI, Khrizanforov MN, Gerasimova TP, Budnikova YH (2024) Carbon dioxide electroreduction and formic acid oxidation by formal nickel(I) complexes of di-isopropylphenyl bis-iminoacenaphthene. Chem Eur J 30:e202400168. https://doi.org/10.1002/chem.202400168
10. Kartashov SV, Saifina AF, Fayzullin RR (2024) Toward the chemical structure of diborane: electronic force density fields, effective electronegativity, and internuclear turning surface properties. J Phys Chem A 128:7284–7297. https://doi.org/10.1021/acs.jpca.4c03492
11. Kartashov SV, Fedonin AP, Fayzullin RR (2024) Electronic force density fields: insights into partial bonds, transition states, and chemical structure evolution. J Phys Chem A 128:7471–7488. https://doi.org/10.1021/acs.jpca.4c03699
12. Kartashov SV, Fedonin AP, Fayzullin RR (2024) Exploring interatomic electron transfer and metal–ligand binding mechanism in trimethylenemethane iron tricarbonyl: insights from potentials per electron and corresponding force density fields. Inorg Chem 63:21994–22008. https://doi.org/10.1021/acs.inorgchem.4c03384
13. Fedonin AP, Kartashov SV, Fayzullin RR (2025) Fermi hole behavior in O–H···O and N–H···S hydrogen bonds: equilibrium points in the electrostatic and total static force fields and the electron density gradient as reference positions for the probe electron. Russ J Gen Chem 95:525–531. https://doi.org/10.1134/S107036322560136X
14. Kartashov SV, Fayzullin RR (2025) Evaluating and interpreting the exchange correlation contributions to the total static and interelectron interaction force densities, with a force-field perspective on the exchange charge density. Phys Chem Chem Phys 27:8521–8539. https://doi.org/10.1039/D5CP00061K
15. Takebayashi S, Ariai J, Kartashov SV, Fayzullin RR, Onoue T, Mibu K, Kang H-B, Ishizu N (2025) From 18- to 20-electron ferrocene derivatives via ligand coordination. Nat Commun 16:6124. https://doi.org/10.1038/s41467-025-61343-7
16. Kartashov SV, Fayzullin RR (2026) Chemical structure and its evolution in terms of the superimposed electrostatic, exchange, and total static force fields, and the role of the electronic forces in atomic charge redistribution. Struct Chem 37:1881–1899. https://doi.org/10.1007/s11224-025-02527-1
17. Kartashov SV, Fayzullin RR (2026) Functional roles of the electronic force fields in supramolecules and molecular crystals. Estimating the exchange-force component

contributions from the inner-crystal electron density. Struct Chem 37:1865–1880. https://doi.org/10.1007/s11224-025-02549-9

18. Kartashov SV, Fedonin AP, Khusnutdinova JR, Fayzullin RR (2026) Challenging the established view of Lewis-type interactions as formulated within quantum chemical topology: an interpretation of Si–Pt and M–Pt (M = Ga, In, and Sn) bonding in terms of electronic force fields. Struct Chem 37:1901–1917. https://doi.org/10.1007/s11224-025-02604-5
19. Kartashov SV, Fayzullin RR (2026) Pseudoatomic charge constraints and force-field flux relations governing local charge redistribution in electron–nuclear systems. An electronic-force-based insight into interatomic binding in diborane. Struct Chem 37:1933–1949. https://doi.org/10.1007/s11224-025-02613-4
20. Kartashov SV, Fayzullin RR (2026) Pseudoatomic charge constraints governing the distribution of the partial charge densities. The atoms and force-field pseudoatoms in the hexagonal and cubic boron nitride crystals. Struct Chem 37:1919–1932. https://doi.org/10.1007/s11224-025-02636-x
21. Kartashov SV, Saifina AF, Fayzullin RR (2026) Structural topology of the vector field of the electronic virial energy density gradient in relation to the electron-transfer-induced responsive phenomenon. Struct Chem 37:1969–1977. https://doi.org/10.1007/s11224-025-02650-z
22. Kartashov SV, Fedonin AP, Fayzullin RR (2026) Atomic charge distribution and chemical bonding in isolated molecules of 3,4-dihydro-1*H*-benzo[*c*][1,2]thiazine 2,2-dioxide derivatives. J Struct Chem 67:713–725. https://doi.org/10.1134/S0022476626040013
23. Saifina AF, Kartashov SV, Fayzullin RR (2026) Anatomy and formation of Br···O=C halogen and nonclassical hydrogen bonds and π···π stacking: insights from the conservative electronic force fields in the molecular crystal and the supermolecule of 1-(5-bromopyridin-2-yl)ethan-1-one. Struct Chem 37:1951–1968. https://doi.org/10.1007/s11224-025-02711-3
24. Kartashov SV, Saifina AF, Andriyanov RYu, Fayzullin RR (2027) Advancing the concept of exchange charge density: a theoretical extension in terms of the Fermi hole density and the development of a form within the local density approximation. Struct Chem. https://doi.org/10.1007/s11224-025-02714-0
25. Kartashov SV, Fayzullin RR (2027) Structural topology of the vector field of the electronic virial energy density gradient in relation to the electron-transfer-induced responsive phenomenon. Part 2: transition states and partial chemical bonds. Struct Chem. https://doi.org/10.1007/s11224-026-02776-8
26. Kartashov SV, Fayzullin RR (2027) Commentary on defining noncovalent and metal-coordination Lewis-type interactions: Lewis acid–base assignment, electrostatic-potential hole

notation, and interatomic charge transfer. Struct Chem. https://doi.org/10.1007/s11224-026-02796-4

27. Kartashov SV, Fayzullin RR (2027) Chemical structure in terms of electronic force fields and their associated local charge densities: an extension of the framework from the Slater to the Ehrenfest formulation. Struct Chem. https://doi.org/10.1007/s11224-026-02844-z
28. Fayzullin RR (2027) Quantum crystallography: a personal perspective on its scope and emerging directions. Struct Chem. https://doi.org/10.1007/s11224-026-02893-4
29. Sini G, Maitre P, Hiberty PC, Shaik SS (1991) Covalent, ionic and resonating single bonds. J Mol Struct THEOCHEM 229:163–188. https://doi.org/10.1016/0166-1280(91)90144-9
30. Shaik S, Maitre P, Sini G, Hiberty PC (1992) The charge-shift bonding concept. Electron-pair bonds with very large ionic–covalent resonance energies. J Am Chem Soc 114:7861–7866. https://doi.org/10.1021/ja00046a035
31. Shaik S, Danovich D, Silvi B, Lauvergnat DL, Hiberty PC (2005) Charge-shift bonding—a class of electron-pair bonds that emerges from valence bond theory and is supported by the electron localization function approach. Chem Eur J 11:6358–6371. https://doi.org/10.1002/chem.200500265
32. Shaik S, Danovich D, Wu W, Hiberty PC (2009) Charge-shift bonding and its manifestations in chemistry. Nat Chem 1:443–449. https://doi.org/10.1038/nchem.327
33. Shaik S, Danovich D, Galbraith JM, Braïda B, Wu W, Hiberty PC (2020) Charge-shift bonding: a new and unique form of bonding. Angew Chem Int Ed 59:984–1001. https://doi.org/10.1002/anie.201910085
34. Dunitz JD, Seiler P (1983) The absence of bonding electron density in certain covalent bonds as revealed by X-ray analysis. J Am Chem Soc 105:7056–7058. https://doi.org/10.1021/ja00362a007
35. Messerschmidt M, Wagner A, Wong MW, Luger P (2002) Atomic properties of N_2O_4 based on its experimental charge density. J Am Chem Soc 124:732–733. https://doi.org/10.1021/ja011802c
36. Tsirelson VG, Shishkina AV, Stash AI, Parsons S (2009) The experimental and theoretical QTAIMC study of the atomic and molecular interactions in dinitrogen tetroxide. Acta Crystallogr, Sect B: Struct Sci 65:647–658. https://doi.org/10.1107/S0108768109028821
37. Vener MV, Medvedev AG, Stash AI, Mikhaylov AA, Prikhodchenko PV, Baravikov DE, Dalinger IL, Churakov AV, Dolgushin FM (2025) The first experimental charge density studies and comparative periodic DFT calculations for crystalline hydrogen peroxide adducts: peculiarities of the HO–OH covalent bond. J Phys Chem Lett 16:10316–10323. https://doi.org/10.1021/acs.jpclett.5c01752

38. Bader RFW, Beddall PM (1972) Virial field relationship for molecular charge distributions and the spatial partitioning of molecular properties. J Chem Phys 56:3320–3329. https://doi.org/10.1063/1.1677699
39. Bader RFW, Nguyen-Dang TT (1981) Quantum theory of atoms in molecules—Dalton revisited. In: Löwdin P-O (ed) Advances in quantum chemistry. Academic Press, pp 63–124. https://doi.org/10.1016/S0065-3276(08)60326-3
40. Bader RFW (1985) Atoms in molecules. Acc Chem Res 18:9–15. https://doi.org/10.1021/ar00109a003
41. Bader RFW (1990) Atoms in molecules: a quantum theory. Clarendon Press. https://doi.org/10.1093/oso/9780198551683.001.0001
42. Bader RFW (1991) A quantum theory of molecular structure and its applications. Chem Rev 91:893–928. https://doi.org/10.1021/cr00005a013
43. Bader RFW (2007) Everyman's derivation of the theory of atoms in molecules. J Phys Chem A 111:7966–7972. https://doi.org/10.1021/jp073213k
44. Bader RFW, Srebrenik S, Nguyen-Dang TT (1978) Subspace quantum dynamics and the quantum action principle. J Chem Phys 68:3680–3691. https://doi.org/10.1063/1.436226
45. Bader RFW (1994) Principle of stationary action and the definition of a proper open system. Phys Rev B 49:13348–13356. https://doi.org/10.1103/PhysRevB.49.13348
46. Bader RFW (2001) The zero-flux surface and the topological and quantum definitions of an atom in a molecule. Theor Chem Acc 105:276–283. https://doi.org/10.1007/s002140000233
47. Bader RFW (1975) Molecular fragments or chemical bonds. Acc Chem Res 8:34–40. https://doi.org/10.1021/ar50085a005
48. Bader RFW, Zou PF (1992) An atomic population as the expectation value of a quantum observable. Chem Phys Lett 191:54–58. https://doi.org/10.1016/0009-2614(92)85367-J
49. Bader RFW, Matta CF (2004) Atomic charges are measurable quantum expectation values: a rebuttal of criticisms of QTAIM charges. J Phys Chem A 108:8385–8394. https://doi.org/10.1021/jp0482666
50. Bader RFW (1998) A bond path: a universal indicator of bonded interactions. J Phys Chem A 102:7314–7323. https://doi.org/10.1021/jp981794v
51. Bader RFW (2006) Pauli repulsions exist only in the eye of the beholder. Chem Eur J 12:2896–2901. https://doi.org/10.1002/chem.200501589
52. Bader RFW (2009) Bond paths are not chemical bonds. J Phys Chem A 113:10391–10396. https://doi.org/10.1021/jp906341r

53. Bader RFW, Stephens ME (1975) Spatial localization of the electronic pair and number distributions in molecules. J Am Chem Soc 97:7391–7399. https://doi.org/10.1021/ja00859a001
54. Fradera X, Austen MA, Bader RFW (1999) The Lewis model and beyond. J Phys Chem A 103:304–314. https://doi.org/10.1021/jp983362q
55. Matta CF, Ayers PW, Cook R (2024) Electron localization-delocalization matrices. Springer. https://doi.org/10.1007/978-3-031-51434-0
56. Parr RG, Yang W (1989) Density-functional theory of atoms and molecules. Oxford University Press. https://doi.org/10.1093/oso/9780195092769.001.0001
57. McWeeny R (1992) Methods of molecular quantum mechanics, 2nd ed. Academic Press.
58. Koch W, Holthausen MC (2001) A chemist's guide to density functional theory, 2nd ed. Wiley. https://doi.org/10.1002/3527600043
59. Slater JC (1951) A simplification of the Hartree-Fock method. Phys Rev 81:385–390. https://doi.org/10.1103/PhysRev.81.385
60. Yang Z-Z, Davidson ER (1997) Evaluation of a characteristic atomic radius by an ab initio method. Int J Quantum Chem 62:47–53. https://doi.org/10.1002/(SICI)1097-461X(1997)62:1<47::AID-QUA5>3.0.CO;2-3
61. Zhao D-X, Yang Z-Z (2014) Theoretical exploration of the potential and force acting on one electron within a molecule. J Phys Chem A 118:9045–9057. https://doi.org/10.1021/jp5020466
62. Tsirelson V, Stash A (2020) Orbital-free quantum crystallography: view on forces in crystals. Acta Crystallogr, Sect B: Struct Sci Cryst Eng Mater 76:769–778. https://doi.org/10.1107/S2052520620009178
63. Martín Pendás A, Francisco E, Gallo Bueno A, Guevara Vela JM, Costales A (2016) Emergent scalar and vector fields in quantum chemical topology. In: Chauvin R, Lepetit C, Silvi B, Alikhani E (eds) Applications of topological methods in molecular chemistry. Springer, pp 131–150. https://doi.org/10.1007/978-3-319-29022-5_6
64. Ferreira L-M, Eaby A, Dillen J (2017) The topology of the Coulomb potential density. A comparison with the electron density, the virial energy density, and the Ehrenfest force density. J Comput Chem 38:2784–2790. https://doi.org/10.1002/jcc.25071
65. Zhao D-X, Yang Z-Z (2014) Investigation of the distinction between van der Waals interaction and chemical bonding based on the PAEM-MO diagram. J Comput Chem 35:965–977. https://doi.org/10.1002/jcc.23570
66. Tsirelson V, Stash A (2021) Developing orbital-free quantum crystallography: the local potentials and associated partial charge densities. Acta Crystallogr, Sect B: Struct Sci Cryst Eng Mater 77:467–477. https://doi.org/10.1107/s2052520621005540

67. Liu S, Ayers PW, Parr RG (1999) Alternative definition of exchange-correlation charge in density functional theory. J Chem Phys 111:6197–6203. https://doi.org/10.1063/1.479924
68. Görling A (1999) New KS method for molecules based on an exchange charge density generating the exact local KS exchange potential. Phys Rev Lett 83:5459–5462. https://doi.org/10.1103/PhysRevLett.83.5459
69. Peluso P, Gatti C, Dessì A, Dallocchio R, Weiss R, Aubert E, Pale P, Cossu S, Mamane V (2018) Enantioseparation of fluorinated 3-arylthio-4,4'-bipyridines: insights into chalcogen and π-hole bonds in high-performance liquid chromatography. J Chromatogr A 1567:119–129. https://doi.org/10.1016/j.chroma.2018.06.060
70. Gatti C, Bruno G (2023) Chemical insights from the source function reconstruction of scalar fields relevant to chemistry. In: Rodríguez JI, Cortés-Guzmán F, Anderson JSM (eds) Advances in quantum chemical topology beyond QTAIM. Elsevier, pp 269–333. https://doi.org/10.1016/B978-0-323-90891-7.00003-7
71. Ayers PW, Levy M (2001) Sum rules for exchange and correlation potentials. J Chem Phys 115:4438–4443. https://doi.org/10.1063/1.1379333
72. Zhao D-X, Zhao J, Yang Z-Z (2020) Partitioning a molecule into the atomic basins and the resultant atomic charges from quantum chemical topology analysis of the Kohn–Sham potential. J Phys Chem A 124:5023–5032. https://doi.org/10.1021/acs.jpca.0c01289
73. Zhao J, Zhu Z-W, Zhao D-X, Yang Z-Z (2023) Atomic charges in molecules defined by molecular real space partition into atomic subspaces. Phys Chem Chem Phys 25:9020–9030. https://doi.org/10.1039/D2CP05428K
74. Liu X-M, Zhao D-X, Yang Z-Z (2025) Transition from noncovalent interaction to covalent bond based on one-electron potential, quantum chemical topology, and molecular face theory. J Phys Chem A 129:6107–6120. https://doi.org/10.1021/acs.jpca.5c01773
75. Guo X, Cong Y, Zhao J, Zhao D, Yang Z (2025) Developing quantum chemical topology for polypeptide charge distributions using Kohn-Sham one-electron potential. Chem Res Chin Univ 41:1121–1132. https://doi.org/10.1007/s40242-025-5150-5
76. Popelier PLA (2001) A fast algorithm to compute atomic charges based on the topology of the electron density. Theor Chem Acc 105:393–399. https://doi.org/10.1007/s002140000224
77. Bader RFW (1980) Quantum topology of molecular charge distributions. III. The mechanics of an atom in a molecule. J Chem Phys 73:2871–2883. https://doi.org/10.1063/1.440457
78. Hernández-Trujillo J, Bader RFW (2000) Properties of atoms in molecules: atoms forming molecules. J Phys Chem A 104:1779–1794. https://doi.org/10.1021/jp994096z
79. Hernández-Trujillo J, Cortés-Guzmán F, Fang D-C, Bader RFW (2007) Forces in molecules. Faraday Discuss 135:79–95. https://doi.org/10.1039/B604996F

80. Mortera-Carbonell AJ, García-García S, Francisco E, Hernández-Trujillo J, Martín Pendás Á (2027) Atomic Ehrenfest forces. Struct Chem. https://doi.org/10.1007/s11224-026-02925-z
81. Jenkins S, Kirk SR, Guevara-García A, Ayers PW, Echegaray E, Toro-Labbe A (2011) The mechanics of charge-shift bonds: a perspective from the electronic stress tensor. Chem Phys Lett 510:18–20. https://doi.org/10.1016/j.cplett.2011.05.023
82. Frisch MJ, Trucks GW, Schlegel HB, Scuseria GE, Robb MA, Cheeseman JR, Scalmani G, Barone V, Petersson GA, Nakatsuji H, Li X, Caricato M, Marenich AV, Bloino J, Janesko BG, Gomperts R, Mennucci B, Hratchian HP, Ortiz JV, Izmaylov AF, Sonnenberg JL, Williams-Young D, Ding F, Lipparini F, Egidi F, Goings J, Peng B, Petrone A, Henderson T, Ranasinghe D, Zakrzewski VG, Gao J, Rega N, Zheng G, Liang W, Hada M, Ehara M, Toyota K, Fukuda R, Hasegawa J, Ishida M, Nakajima T, Honda Y, Kitao O, Nakai H, Vreven T, Throssell K, Montgomery JA (Jr), Peralta JE, Ogliaro F, Bearpark MJ, Heyd JJ, Brothers EN, Kudin KN, Staroverov VN, Keith TA, Kobayashi R, Normand J, Raghavachari K, Rendell AP, Burant JC, Iyengar SS, Tomasi J, Cossi M, Millam JM, Klene M, Adamo C, Cammi R, Ochterski JW, Martin RL, Morokuma K, Farkas Ö, Foresman JB, Fox DJ (2016) Gaussian 16.
83. Dunning TH (1989) Gaussian basis sets for use in correlated molecular calculations. I. The atoms boron through neon and hydrogen. J Chem Phys 90:1007–1023. https://doi.org/10.1063/1.456153
84. Kendall RA, Dunning TH, Harrison RJ (1992) Electron affinities of the first-row atoms revisited. Systematic basis sets and wave functions. J Chem Phys 96:6796–6806. https://doi.org/10.1063/1.462569
85. Prascher BP, Woon DE, Peterson KA, Dunning TH (Jr), Wilson AK (2011) Gaussian basis sets for use in correlated molecular calculations. VII. Valence, core-valence, and scalar relativistic basis sets for Li, Be, Na, and Mg. Theor Chem Acc 128:69–82. https://doi.org/10.1007/s00214-010-0764-0
86. Bartlett RJ, Purvis GD (1978) Many-body perturbation theory, coupled-pair many-electron theory, and the importance of quadruple excitations for the correlation problem. Int J Quantum Chem 14:561–581. https://doi.org/10.1002/qua.560140504
87. Purvis GD (III), Bartlett RJ (1982) A full coupled-cluster singles and doubles model: the inclusion of disconnected triples. J Chem Phys 76:1910–1918. https://doi.org/10.1063/1.443164
88. Scuseria GE, Janssen CL, Schaefer HF (III) (1988) An efficient reformulation of the closed-shell coupled cluster single and double excitation (CCSD) equations. J Chem Phys 89:7382–7387. https://doi.org/10.1063/1.455269

89. Lu T, Chen F (2012) Multiwfn: a multifunctional wavefunction analyzer. J Comput Chem 33:580–592. https://doi.org/10.1002/jcc.22885
90. Lu T (2024) A comprehensive electron wavefunction analysis toolbox for chemists, Multiwfn. J Chem Phys 161:082503. https://doi.org/10.1063/5.0216272
91. Zhang J, Lu T (2021) Efficient evaluation of electrostatic potential with computerized optimized code. Phys Chem Chem Phys 23:20323–20328. https://doi.org/10.1039/D1CP02805G
92. Müller AMK (1984) Explicit approximate relation between reduced two- and one-particle density matrices. Phys Lett A 105:446–452. https://doi.org/10.1016/0375-9601(84)91034-X
93. Keith TA (2019) AIMAll.
94. Fock V (1930) Näherungsmethode zur Lösung des quantenmechanischen Mehrkörperproblems. Z Phys 61:126–148. https://doi.org/10.1007/BF01340294
95. Roothaan CCJ (1951) New developments in molecular orbital theory. Rev Mod Phys 23:69–89. https://doi.org/10.1103/RevModPhys.23.69
96. Chai J-D, Head-Gordon M (2008) Long-range corrected hybrid density functionals with damped atom–atom dispersion corrections. Phys Chem Chem Phys 10:6615–6620. https://doi.org/10.1039/b810189b
97. Bartashevich E, Tsirelson V (2026) Chemical bonds characterization by one-electron potentials, interatomic surfaces and related descriptors. Coord Chem Rev 549:217243. https://doi.org/10.1016/j.ccr.2025.217243
98. Mortera-Carbonell AJ, Hernández-Trujillo J, Francisco E, Martín Pendás A (2026) Chemical information from the Ehrenfest force field based on reduced density matrix functional theory. J Comput Chem 47:e70331. https://doi.org/10.1002/jcc.70331

ORCID

Sergey V. Kartashov: https://orcid.org/0000-0003-3875-1953

Robert R. Fayzullin: https://orcid.org/0000-0002-3740-9833